CHAPTER

24 Embedded Carbon Nanotube Sensor Thread for Structural Health Monitoring and Strain Sensing of Composite Materials

Adam Hehr, Yi Song, Bolaji Suberu, Joe Sullivan, Vesselin Shanov, Mark Schulz
University of Cincinnati, College of Engineering and Applied Science, Cincinnati, Ohio USA

CHAPTER OUTLINE

24.1 INTRODUCTION

The need for speed—i.e. higher performance and efficiency—is driving the increased use of advanced composite materials in high-cost defense and commercial applications (see Fig. 24.1). These materials provide high specific strength and high performance, but ensuring material safety and reliability is a challenge. Currently, over 80% of structural commercial aircraft inspections are done visually [1] (Federal Aviation Administration of the USA, 1997), and visual inspection continues to be the leading technique for composite aircraft [2]. However, these external visual

Nanotube Superfiber Materials. http://dx.doi.org/10.1016/B978-1-4557-7863-8.00024-4

FIGURE 24.1

SHM technology may increase aircraft reliability, safety, and efficiency and reduce operating costs of aircraft. (For color version of this figure, the reader is referred to the online version of this book.)

Sources: F-22 photo taken by Rob Shenk [4], Apache photo courtesy of U.S. Army and taken by Tech. Sgt. Andy Dunaway [5], 787 photo taken by wiki user, Spaceaero2 [6].

inspections do not work reliably well with laminated composite materials due to many failure modes manifesting and progressing from within the material, such as matrix cracking and ply delamination [3].

An example of unseen ply delamination in a laminated composite from an impact can be seen in Fig. 24.2. It should be pointed out that the external indent is very small compared to the internal damage area and that there is no obvious evidence of this internal damage from the exterior. As a consequence of poor failure mode detection

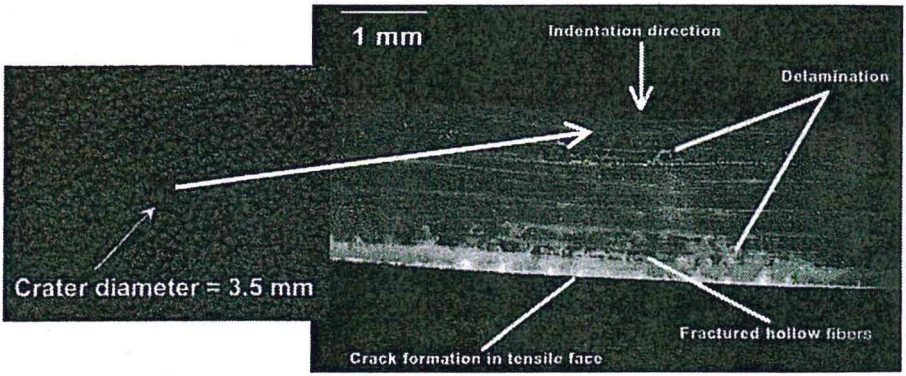

FIGURE 24.2

Ply delamination from an external impact. The composite in the figure would have a similar small indent where there is no obvious evidence of internal damage from the exterior.

Sources: These photos taken and combined from [7] and [8] with permission. Exterior impact photo reprinted from Springer and JOM's The development of multifunctional composite material for use in human space exploration beyond low-earth orbit *is given to the publication in which the material was originally published with kind permission from Springer Science and Business Media. Composite figure reprinted from* A hollow fibre reinforced polymer composite encompassing self-healing and enhanced damage visibility *with permission from Elsevier.*

in these materials, material reliability has limited or slowed use in certain applications, such as in commercial air flight, where reliability and safety are of utmost importance.

In order to inspect composite materials in a more effective manner, costly nondestructive techniques such as ultrasonic inspection and somewhat qualitative tap tests have been employed [3]. Besides being costly in capital and accuracy, these techniques are time consuming and the aircraft must be taken out of service for inspection. As a result, planes will be inspected less frequently and thorough inspections can only take place when the plane is out of commission for an extended period. However, by building sensors into the composite material, assessment can be done in real time, can be more accurate, and would be less costly in time, labor, and operator/passenger safety.

The idea of building damage sensing and detection into composite materials is not a new one. Researchers began building traditional strain gauges into composites several decades ago; however, these embedded strain sensors create large stress concentrations in the material, which degrades the fatigue strength and longevity of the material [9]. Additionally, many of the embedded sensor schemes were not dense enough to monitor critical complex geometries like in the F-22 Raptor wings (Fig. 24.3), and the sensor's design life is much shorter than the structure that is being monitored [10]. To mitigate these large stress concentrations, increased sensor density, and increased sensor longevity, small robust continuous sensors have begun to attract attention. Currently, the leading technology that meets these characteristics of small, robust, and easily

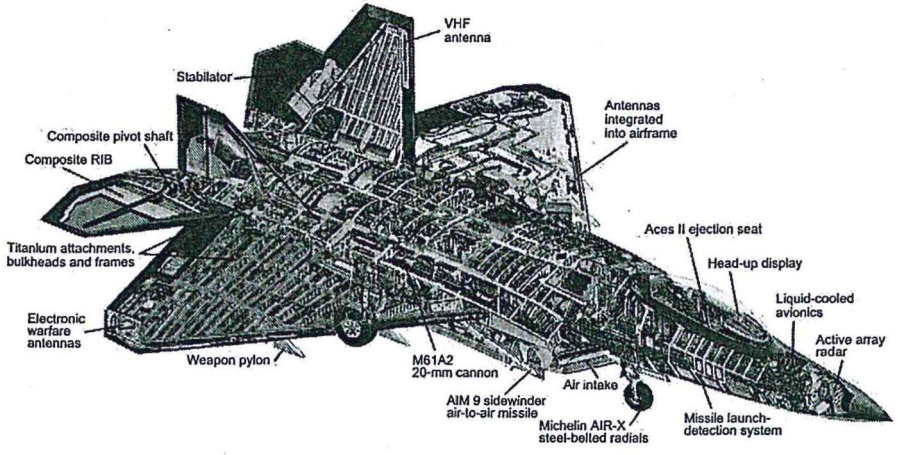

FIGURE 24.3

Internal rib structure of F-22 Raptor. Monitoring the composite ribs in the wings and external composite panels becomes difficult with their complex geometries. (For color version of this figure, the reader is referred to the online version of this book.)

Source: This image is approved by US DoD for use.

distributed is fiber-optic cabling. However, fiber-optic cabling interrogation equipment is currently very expensive, i.e. on the order of 20,000 USD per interrogator. Thus, fiber-optic cabling only becomes feasible if the sensing system is large [10]. Despite this high cost, fiber-optic cable is extremely robust to environmental conditions, can undergo frequent loading, and is immune to electromagnetic radiation [10]. However, this high cost of operation has led researchers to explore other small, robust, and fiber/tape-like options, such as carbon nanotube (CNT) film/sheet [11], fiber [12], thread [13–15] and the carbon fiber itself [16]. In the past 4 years, the University of Cincinnati (UC) Nanoworld Laboratories has been investigating miniature sensors using CNT thread and tape (tape is flat adhesive-backed CNT sheet or thread). As a result, the sensing element is much smaller than conventional sensors [17–29], would be minimally invasive if built into the material, can be used in complex geometries, would withstand the life of the structure, and could improve the material besides damage sensing.

CNT thread spun from a CNT forest has a piezoimpedance property (electrical impedance based on *R, L, C* properties changes with strain/stress). Thus, CNT thread can be used to measure internal material strain along with detecting damage in composite materials. This change in impedance comes from the lateral overlap and end gaps between the individual nanotubes in the thread due to strain. As a result, the resistance increases with strain and if the thread breaks due to damage in the composite, the impedance becomes large. The first use of CNT sensor thread to detect damage in composite materials was performed at the UC [14,30,31] by Dr Jandro Abot working with the Nanoworld Group at UC. Some of the CNT materials produced in Nanoworld Laboratories can be seen in Fig. 24.4. It should be noted that CNT sheet has similar properties, but its use as a structural health monitoring (SHM) sensor will not be discussed in detail in this chapter. Instead, the primary focus will be on CNT thread.

As mentioned before, these embedded CNT materials have the potential to improve standard composite materials in many ways other than self-sensing, often called multifunctional features. The following are the potential multifunctional features if CNT thread is added to traditional polymeric composite materials:

1. *Strain sensing:* CNT thread is piezoresistive so it can be used to measure strain besides detecting damage. CNT thread also has capacitance, so its impedance decreases significantly (less than copper wire) at high frequencies, which, in turn could allow increased sensitivity to damage/strain [32].
2. *Thermal sensing:* CNT thread can be used as a temperature sensor [13].
3. *Moisture sensing:* CNTs have been used previously as capacitive moisture sensors [33], which would provide valuable information about added water weight and icing risk to the composite.
4. *Oxidation sensing:* Carbon materials easily oxidize or degrade at high temperatures [34], therefore, these materials are limited in their application.

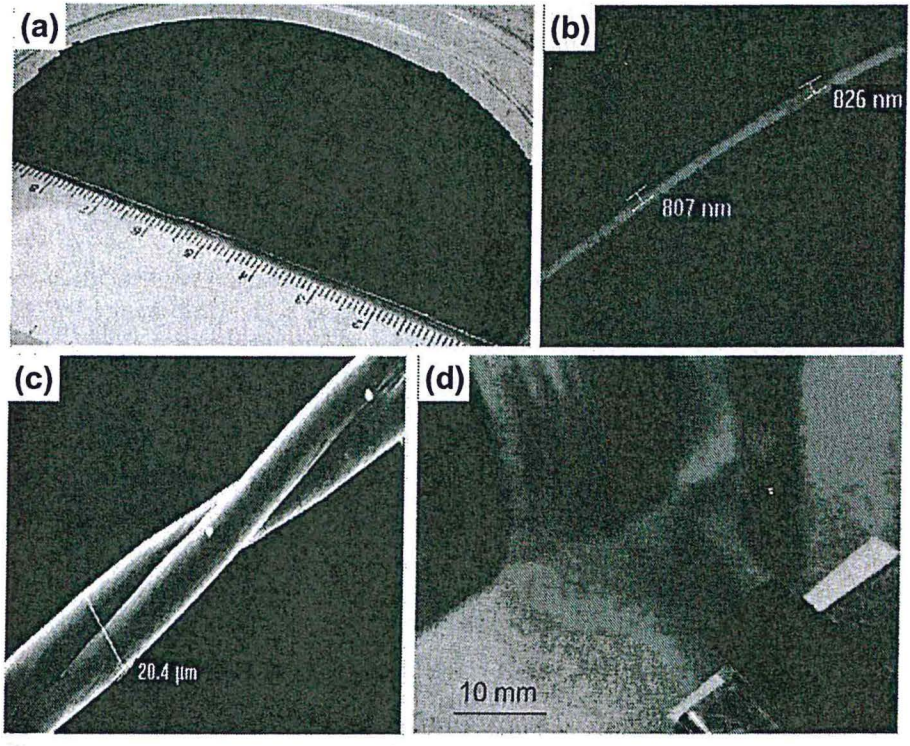

FIGURE 24.4

CNT materials: (a) vertically aligned CNT array, (b) nanothread produced under the microscope, (c) two-ply yarn, and (d) sheet produced by the University of Cincinnati. These materials can be pure CNT or infiltrated with polymer. (For color version of this figure, the reader is referred to the online version of this book.)

Yet, by utilizing the electrochemical properties of CNTs, corrosion or oxidation could be measured and tracked similar to metals by measuring the electrical resistivity [35].

5. *Increased strength and stiffness:* Composite strength will increase based on the volume fraction of CNT thread in comparison to epoxy [36].
6. *Increased damping:* CNT threads and materials exhibit damping on the same or larger order of magnitude of epoxy damping. Thus, CNT integration will enhance or maintain current material damping. Others have used CNTs to improve damping in composite materials already [37,38].
7. *Damage limiting:* Carbon fibers break at small strain (~1%) [39]. CNT thread has higher strain to failure (~3–5%) and will self-limit damage by absorbing strain energy, which holds the composite together and makes it resilient. Others have proven composite toughening with CNTs [40,41].

8. *Improved transport:* CNT thread has high thermal [42] and electrical conductivity in plane, which will moderately improve the properties of the composite.
9. *No significant added weight or size:* There is almost no added mass or volume of the sensor thread and simple lightweight instrumentation is used to interrogate/measure the sensor material.
10. *Other multifunctional areas:* Electrical grounding [40], Electro-magnetic interference (EMI) shielding [43], hydrophobic material [44], energy harvesting [45,46], and self-healing [47].

Enhancements of strength, stiffness toughness, and damping will be made by replacing unneeded epoxy between neighboring fibers with small-diameter CNT thread. This idea is called *High Volume Fraction of CNT Thread* and an invention disclosure was filed for an approach to integrate CNT thread into carbon fibers [36].

The remainder of this chapter focuses on work done with CNT threads for composite material SHM for embedded sensing proof-of-concept work, an assessment of CNT thread strain sensor performance, potential designs for using embedded CNT thread on current aircraft, some explored multifunctional areas, and future work.

24.2 EMBEDDED SENSING PROOF OF CONCEPT

The UC began using CNT thread as a damage and strain sensing element in the 2008–2010 time frame. Several proof-of-concept experiments were done with the CNT thread, and one of the first experiments was embedding the thread into an epoxy beam, which was strained in a four-point bending test rig [48]. This epoxy beam and embedded thread can be seen in Fig. 24.5 along with the schematic of the test in Fig. 24.6.

A four-point bending test was done over a three-point bending test because the strain field should theoretically be constant between each load point. Also, this test assumed that the thread lies in the same plane with respect to the neutral axis. This measurement approach provided a basis for calculating a reasonable estimate of the gauge factor for the embedded thread. In this test, strain and stress within the beam were estimated from Bernoulli beam theory.

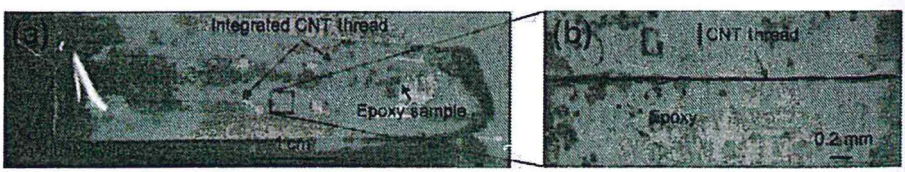

FIGURE 24.5

Epoxy beam with embedded carbon nanotube: (a) thread in epoxy beam; (b) zoomed-in region from (a) showing thread. (For color version of this figure, the reader is referred to the online version of this book.)

Source: From [48] with permission from the publisher.

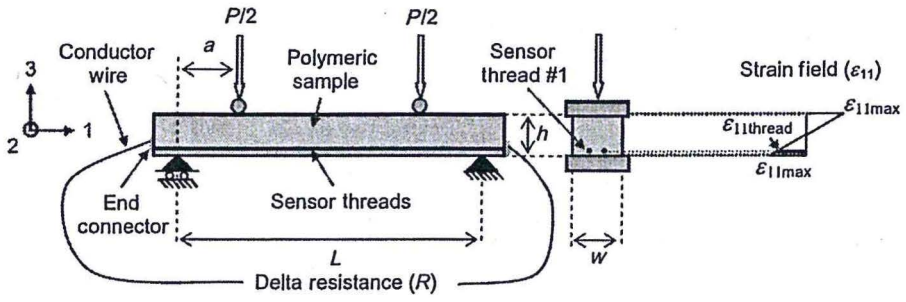

FIGURE 24.6

Schematic of epoxy brick with beam loading conditions, i.e. a four-point bending test. This loading condition creates a constant strain condition between load points. (For color version of this figure, the reader is referred to the online version of this book.)

Source: From [48] with permission from the publisher.

During the experiment, the epoxy was loaded up to about 1% strain at the top surface of the beam to avoid cracking and early failure. However, after several loading cycles, the sample did begin to crack/break. Nonetheless, this test provided a baseline estimate of resistance response of CNT thread to strain while studying consecutive loading cycles of strain. The resistance response from strain can be seen in Fig. 24.7 for a single cycle and for six cycles. Note that the resistance response tracks the stress response fairly well in shape and trends.

The gauge factor can be estimated from this test setup. Thus, the calculated gauge factors for the loading cycles seen above can be seen below in Fig. 24.8. It appeared that the thread consistently had two zones of sensitivity and that the second zone was fairly consistent in response. This experiment estimated a gauge factor of

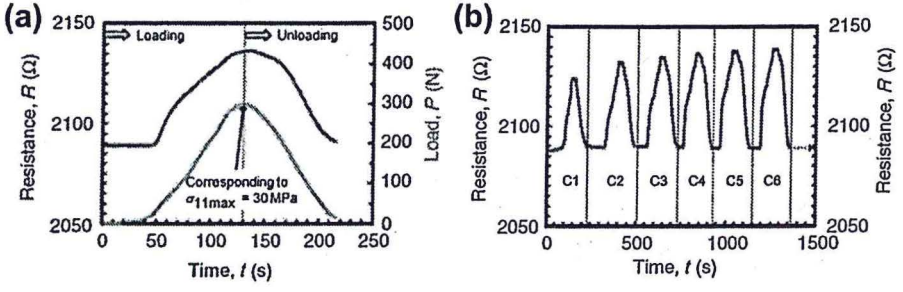

FIGURE 24.7

Resistance response of embedded CNT thread to an applied stress: (a) single cycle and (b) several strain cycles. (For color version of this figure, the reader is referred to the online version of this book.)

Source: From [48] with permission from the publisher.

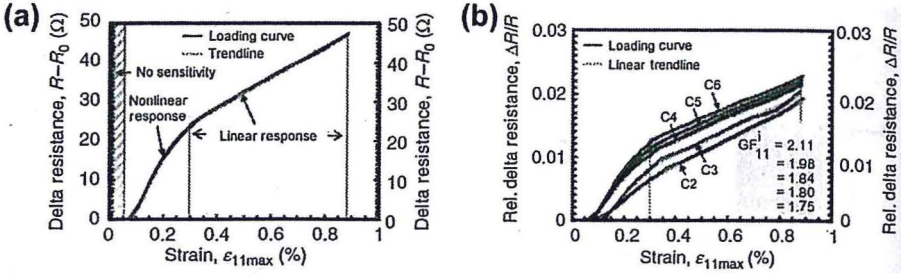

FIGURE 24.8

Analysis of embedded thread resistance response to strain. (a) Sensitivity or gauge factor for a single loading cycle and (b) consistency of the gauge factor to multiple loading cycles. (For color version of this figure, the reader is referred to the online version of this book.)

Source: From [48] with permission from the publisher.

around 1.8–2, which is on the order of foil-type strain gauge performance. However, recent result of thread, which is not embedded in any composite or epoxy, has a far smaller response, as will be seen later in the chapter. This difference between experiments is not well understood and may be due to the effect of epoxy reducing the strain of the thread and is still being investigated.

In addition to embedding CNT thread into epoxy beams, CNT thread sensors were also embedded into composite materials themselves to measure the onset of damage, specifically mode I (crack opening) and II (in-plane shear/sliding) delamination [49]. In order to initiate and measure mode II delamination, a multi-ply composite beam was fabricated with a CNT thread stitched transversely through the ply layers and down the beam, as seen in Fig. 24.9. This composite beam was then loaded to failure in a three-point bending test fixture while the resistance response of the CNT thread was measured. The resistance response from this mode II delamination initiation test can be seen in Fig. 24.9, and it should be highlighted that the thread breakage is directly correlated to the onset of delamination. This test was done with both E-glass fiber composites and IM7/977-3 carbon fiber composites, and both materials had similar CNT thread resistance responses. However, it should be noted that the CNT thread sensors in the carbon fiber composite were coated with a polyurethane coating prior to stitching. This coating was used for electrical isolation of the CNT thread from the carbon fibers, but the interface between the fiber and coating was not well understood prior to the experiment. Consequently, confidence in electrical isolation was low in the carbon fiber composite test.

Mode I delamination was also done on a composite beam with transversely stitched CNT threads. To simulate crack opening, the composite beam's plies were pulled apart; specifically, a crack was built into the beam near the center and a load was applied on the edge of the material to force a crack to propagate along the ply layer interface. While this crack propagated along the interface,

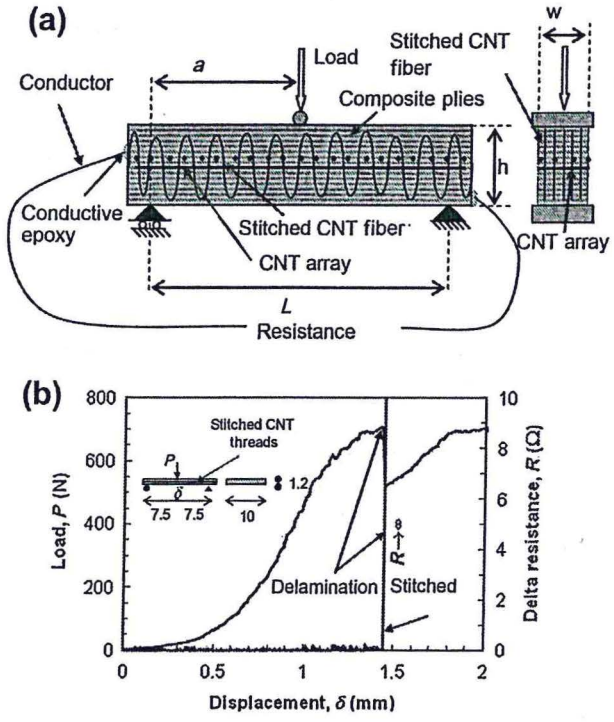

FIGURE 24.9

Three-point bend test for detecting in-plane damage/delamination in laminated composites. (a) Schematic of longitudinal and transverse cross-sections of a laminated composite beam sample instrumented with in-plane sensor arrays and transversely stitched sensor tapes. When the tapes are broken, their resistance increases. (b) Load vs deflection and thread delta resistance (difference between actual and initial resistance) vs deflection curves for an IM7/977-3 10-ply unidirectional composite subjected to three-point bending. It can be seen that one of the sensor threads captures the delamination exactly at its onset since the discontinuity in both curves occurs simultaneously. (For color version of this figure, the reader is referred to the online version of this book.)

Source: Reprinted from Delamination with carbon nanotube thread in self-sensing composite materials *with permission from Elsevier.*

the resistance responses of the embedded threads were monitored to identify crack location. Besides monitoring the CNT threads, a reference foil-type strain gauge was also mounted to the plies as a reference for comparison. The resistance response from these embedded threads and reference strain gauge can be seen in Fig. 24.10 along with a schematic of the experimental design. As seen from the resistance response of the embedded threads, each thread identifies, in a separable manner, when the crack reaches and passes through the material.

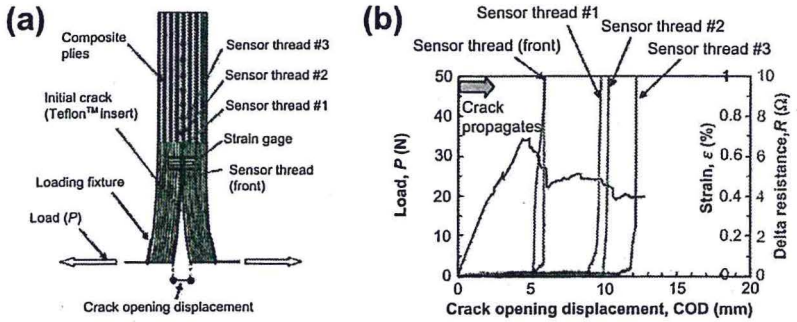

FIGURE 24.10

Detection of mode I delamination in laminated composite materials. (a) Schematic of double-cantilevered beam with a precrack between the central plies. The beam is mounted with a strain gauge to measure crack growth while the plies are pulled apart. (b) Resistance response of the strain gauge and embedded CNT thread from the induced crack along with the applied crack opening load. Note that the foil strain gauge and the closest CNT thread sensor to the strain gauge identify the crack's propagation within a close proximity. Additionally, all the subsequent CNT thread sensors identify when the crack reaches that part of the composite. (For color version of this figure, the reader is referred to the online version of this book.)

Source: Reprinted from Delamination with carbon nanotube thread in self-sensing composite materials *with permission from Elsevier.*

In addition to showing potential as a piezoresistive strain and damage sensor, the CNT thread can also act as an infrared (IR) damage sensor [50]. If a polymer is reinforced with CNT thread, and the thread is powered by a DC or an AC voltage, it will start Joule heating. This heat can then be measured with an IR camera to see if the thread is intact. If no heat signature is detected, then the thread has broken internal to the structure, which may imply damage. This concept is demonstrated in Fig. 24.11 for two embedded parallel threads. One thread is hooked up to a DC voltage, while the other has no electrical load applied. This approach could act as a stand-alone sensing method or a parallel method to confirm piezoresistive measurements. The schematic in Fig. 24.11 illustrates how this technique could be scaled up to an actual composite in use. It should also be noted that the temperature can remain below 30 °C for measurement purposes, which is safe for composite materials.

24.3 CNT SENSOR THREAD PERFORMANCE

Since Nanoworld Laboratories began sensing strain and damage in polymeric composites with CNT thread, a few other researchers have begun to perform work along the same lines [13,15]. However, no CNT thread strain and damage sensing literature today rigorously examines "how good" the CNT thread strain sensor is

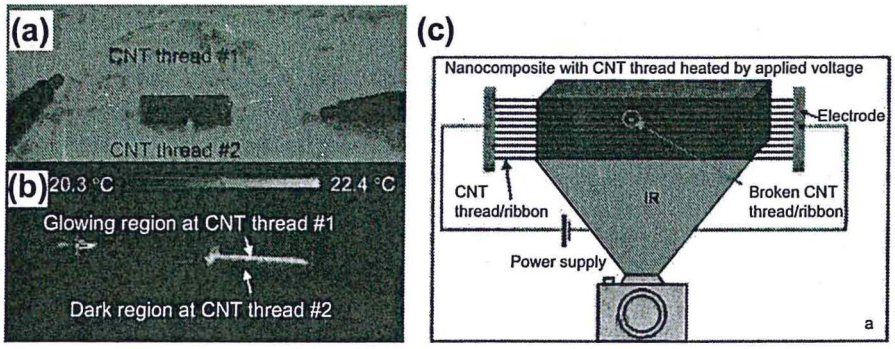

FIGURE 24.11

Remote damage detection with IR thermography. (a) Ambient light photo of two embedded CNT threads with one thread powered with a DC signal; (b) IR image of the same embedded threads, yet it is obvious only one thread is still "intact"; and (c) schematic of SHM of a polymer nanocomposite instrumented with CNT thread using the IR camera for ease in inspection. (For color version of this figure, the reader is referred to the online version of this book.)

Source: From [49] and [50] with permission from the publisher.

performancewise. Consequently, recent efforts at Nanoworld Laboratories have begun to examine the performance of these sensors when they are embedded and not embedded in a polymeric material. The specific areas of performance, which would typically be found on a strain sensor calibration sheet, are listed and defined below.

- Sensitivity: Due to the parameter of strain, sensitivity is essentially the gauge factor for piezoresistive strain sensors.
- Hysteresis: Hysteresis is when there is a dynamic or changing lag or lead in a response from the input. Consequently, things do not behave in a linear manner. Typically, a good sensor is one that demonstrates little to no hysteresis.
- Consistency: Consistency or repeatability here implies accurately measuring the same induced strain consecutively. This can be done by examining what the resistance of the strain gauge is at a particular strain value or by measuring the net change in resistance per strain cycle. In other words, consistency can be analyzed by studying the consistency of the gauge factor for several strain cycles. This gauge factor analysis was done to separate out stability problems, as will be seen and discussed later.
- Stability: As mentioned in the above bullet, stability is an area that requires much attention itself. Stability here implies measurement of drift and variance in the measurement at a particular strain vs time.
- Bandwidth: Bandwidth here implies the maximum (or minimum) frequency of strain that can be confidently measured by the sensor.

Currently, these performance areas have been explored when the CNT thread has not been embedded into any polymeric material. This was primarily done as a benchmark for comparison when the thread was embedded into a polymeric material or any other material for that matter. As a result, all the following performance data is exclusively for nonembedded CNT thread. However, it should be noted that embedded experiments are still in the works and will be carried out. The following subsections will discuss each of these areas in more detail.

24.3.1 Sensitivity (gauge factor)

As mentioned in the above section, sensitivity here implies the gauge factor due to the sensor being used to measure strain. Gauge factor is defined as shown in Eqn (24.1). Thus, the gauge factor can be found by rearranging Eqn (24.1) into a linear equation and fitting a line against the normalized change in resistance ($\Delta R/R_0$) and strain (ε). Consequently, a confident measurement of strain, resistance, and change in resistance needs to be made in order to obtain an accurate gauge factor estimate.

$$\text{Gauge factor (GF)} = \frac{\Delta R}{R_0}\frac{1}{\varepsilon} \tag{24.1}$$

In order to confidently measure the normalized change in resistance and strain, a custom-designed tensile test coupon combined with a custom-designed Wheatstone bridge circuit were utilized. This custom-designed coupon with detailed components can be seen in Fig. 24.12. This coupon was designed within the limits

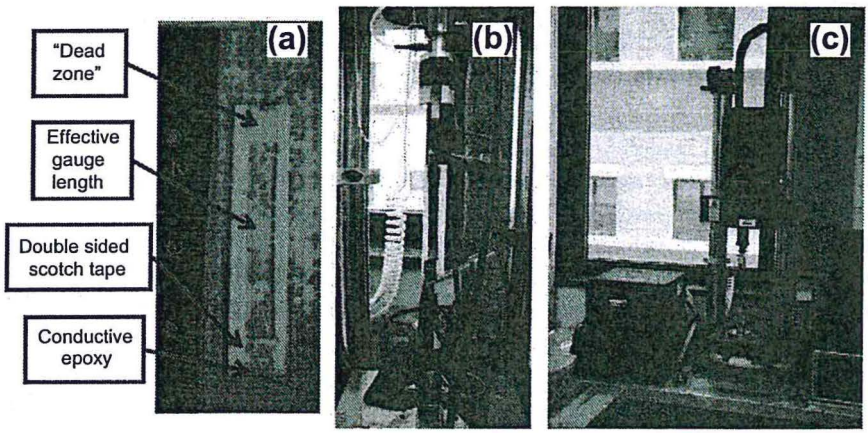

FIGURE 24.12

Sensitivity analysis approach. (a) Sensing sample for making resistance measurements, (b) sensing sample loaded into the grips of the Instron 5948 tensile testing machine, and (c) the Instron 5948 used in these experiments located at Nanoworld Laboratories. (For color version of this figure, the reader is referred to the online version of this book.)

of a high-precision tensile tester at Nanoworld Laboratories, the Instron 5948 (see Fig. 24.12), to maximize the effective gauge length compared to the length of the thread under the machine's grip, called the dead zone in the figure. This approach was taken because (1) strain is calculated by utilizing the displacement output of the moving head of the tensile testing machine and (2) this longer length of thread allowed more thread to be strained, which, in turn, allowed more thread to undergo a change in resistance. In other words, a more confident gauge factor can be measured with a longer effective gauge length. However, from current coupon geometries, an underestimate in the gauge factor of nearly 50% is possible. However, it is assumed that this estimate error is much lower due to the fact that the thread does not strain far into the grip. It should also be noted that the thread is insignificantly stiff relative to the test machine fixture, thus minimal deformation takes place within the gripping structure of the tensile testing machine. Instead, most deformation will take place within the thread. It should also be noted that this strain estimate technique is utilized because using a noncontact video extensiometer to noninvasively measure the thread's strain would be very difficult. To ensure that these assumptions were indeed valid, and they are for the most part, a benchmark gauge factor measurement was done with small-diameter copper wire. Despite the potential for error, this strain measurement approach provides a ballpark estimate in order to draw correlations and perform analysis.

In order to confidently measure the change in resistance, a Wheatstone bridge circuit was utilized as seen in Fig. 24.13. This approach confidently measures the change in resistance because the measurement is a null measurement, or a measurement referenced to zero. Consequently, it is easier to detect small perturbations because the measurement essentially has zero mean. This resistance measurement approach is not as precise as a four-wire measurement, yet the signal to noise ratio is much larger, which, in turn, allows a more accurate resistance change

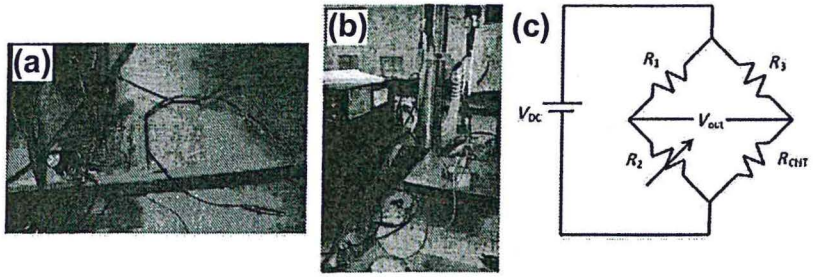

FIGURE 24.13

Wheatstone bridge circuit for resistance measurement. (a) Custom-built Wheatstone bridge circuit for balancing CNT thread against known resistor behavior, (b) custom circuit hooked up to strained specimen in Instron 5948, and (c) schematic of Wheatstone bridge circuit with R_{CNT} representing the CNT thread. This circuit is a null measurement approach to measuring resistance. (For color version of this figure, the reader is referred to the online version of this book.)

measurement to be made [51]. A custom circuit was built with interchangeable balance resistors because (1) CNT thread resistance is not very consistent from thread to thread and this circuit was to be used on more than one thread and (2) a CNT thread can be used as a balance resistor to separate out thermal fluctuations in the testing room. More details on thermal fluctuations and using a CNT thread as a balance resistor will be discussed in the Section 24.3.4. It should be noted, however, that a four-wire measurement approach was done initially with a high-precision data acquisition (DAQ) device, and many of the results presented here were made with a four-wire measurement. This measurement approach was able to fully capture the resistance change due to the high resolution of the DAQ, but this technique does not provide temperature compensation. Thus, short test time measurements could be easily and confidently made with a four-wire technique, such as estimating the gauge factor.

As mentioned before, to validate the assumptions of the tensile test coupon used to estimate the gauge factor, a 90-μm-diameter copper wire's gauge factor was estimated using the same tensile test coupon design as seen in Fig. 24.12. The typical response of copper wire during these tests can be seen in Fig. 24.14. As seen in the figure, the copper wire's gauge factor is correlated with the elastic or linear range of the material. Four samples of copper were used to obtain a mean gauge factor estimate of 2.2 with a standard deviation of 0.66. It is hypothesized that the error here was large because the wire's resistance is incredibly small ($\approx 0.5\ \Omega$) and the change is even smaller. Thus, a precise estimate is difficult to make. Nonetheless, an average of 2.2 is within reasonable bounds of the theoretical response of around 2.1, so it appeared that the tensile test coupon had the potential to obtain a reasonable gauge factor estimate. This theoretical gauge factor response for a cylindrical homogenous material can be seen below in Eqn (24.2), and this equation is animated in Fig. 24.15 to obtain this theoretical value. It should be highlighted that a value of close to 2 was expected because most commercial foil-type strain gauges are made of copper alloys, which have gauge factors on the order of 2.

$$\mathrm{GF}_l = 1 + 2\gamma + \pi_l E \cdot (1 - \gamma) \tag{24.2}$$

where

- γ is the Poisson ratio
- E is the modulus of elasticity
- π is the piezoresistivity constant

The gauge factor for as-spun CNT thread can comparatively be seen in Fig. 24.16. From the figure, two linear zones can be seen that appear to be correlated to the knee in the stress–strain curve of the thread. It should also be highlighted that the elastic region for the stress–strain curve and resistance–strain of the thread is around 1% strain, which is much larger than the elastic region of standard engineering materials and around the breaking strain of many polymeric composites. Thus, this sensor has the potential to measure strains close to material failure.

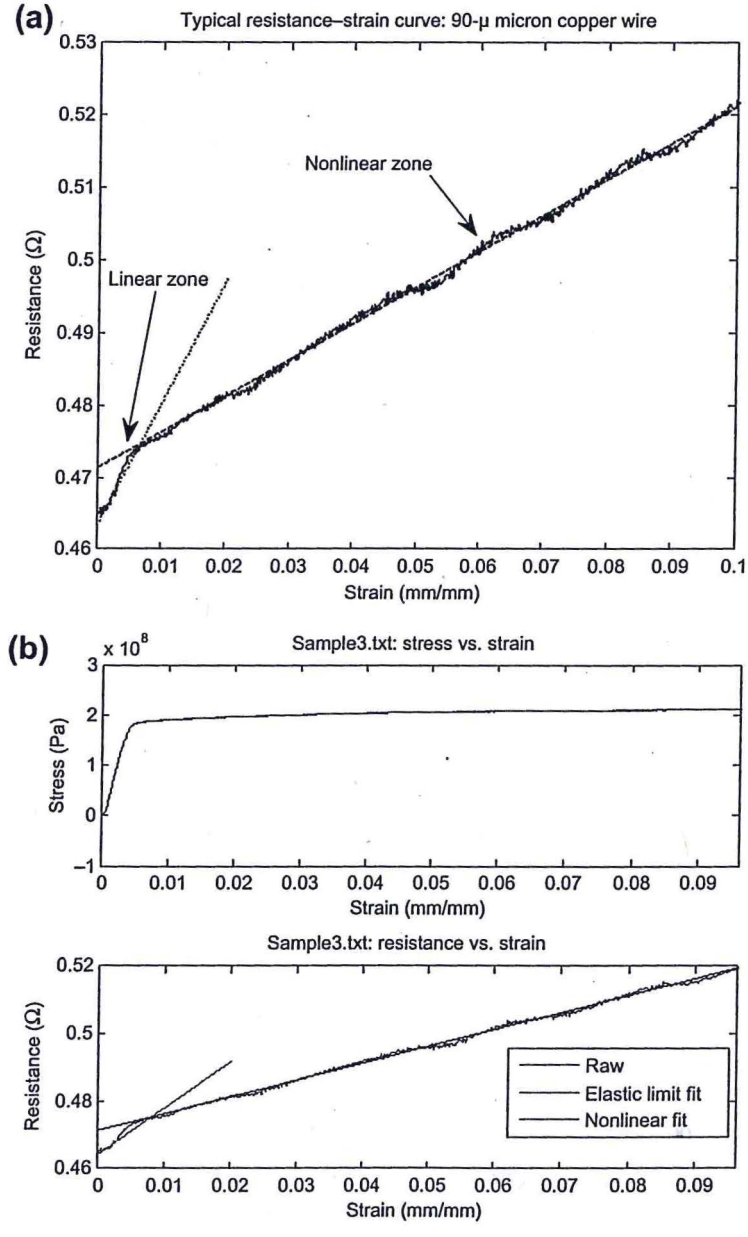

FIGURE 24.14

The resistance response from strain of a 90-μm copper wire. (a) Representative resistance response of copper wire while strained to failure and (b) correlation of linear zone on stress–strain plot with the linear piezoresistive response of the copper. (For color version of this figure, the reader is referred to the online version of this book.)

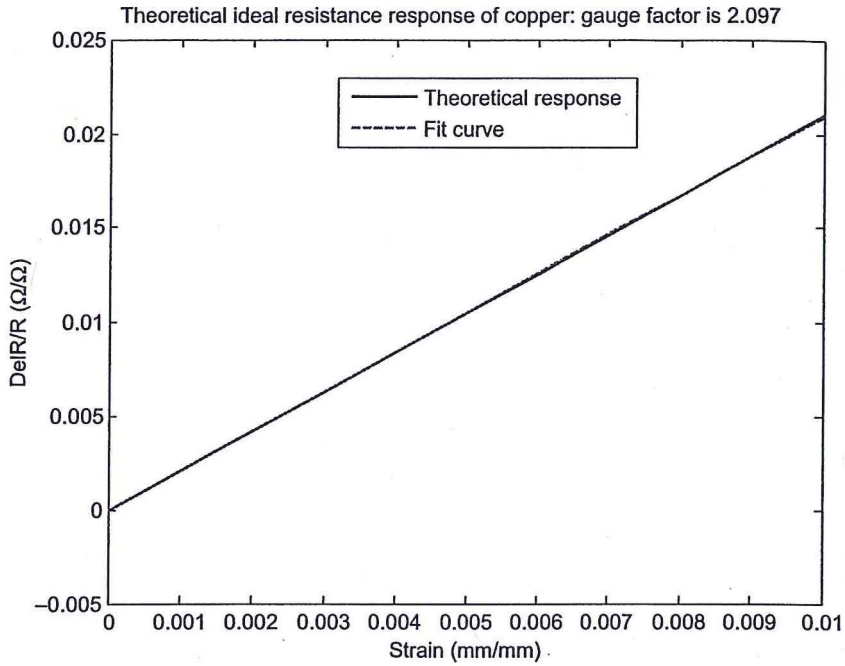

FIGURE 24.15

Theoretical response of 90-μm copper wire to applied strain, assuming that the material remains linear up to 1% strain. A line fit was done because the theoretical relationship is slightly nonlinear. (For color version of this figure, the reader is referred to the online version of this book.)

Although as-spun CNT thread has a large linear range, the gauge factor is typically around 0.2–0.4. This is roughly 10–20% of the sensitivity of copper. It should also be pointed out that CNT thread does not obey the piezoresistive model for a homogenous cylinder as seen in Eqn (24.2). Instead, a given CNT thread is made up of thousands of individual tubes. Thus the piezoresistive effect is suspected to be dominated by these interfaces between the CNTs as seen in CNT film [52]. It is suspected that these interfaces dominate the sensitivity because high Poisson ratios have been reported in CNT thread [53] combined with the gauge factor being less than 1. In other words, CNT thread does not agree with Eqn (24.2). Thus, it could be possible that the piezoresistive coefficient for the radial and lengthwise directions may be counteracting each other. More investigation should be done to prove this hypothesis and to improve fundamental understanding behind this response behavior.

Despite an incomplete understanding of the physical mechanisms behind CNT thread's piezoresistive response, the gauge factor was investigated as a function of the thread's geometry, i.e. the twist angle. This was done to attempt to improve

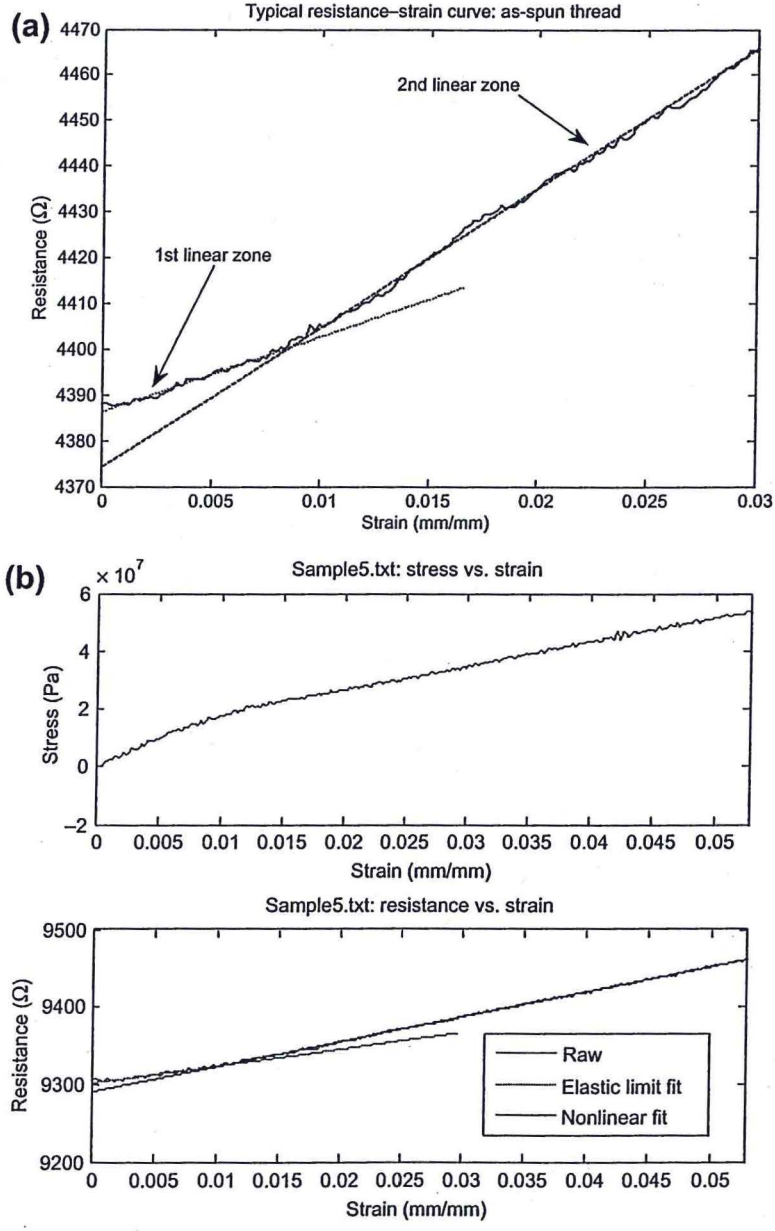

FIGURE 24.16

Resistance response of CNT thread from strain. (a) Illustration of typical resistance response of CNT thread to applied strain and (b) resistance response with synchronized stress–strain curve to illustrate the correlation between the linear sensing zones and linear stress–strain zones of the thread. (For color version of this figure, the reader is referred to the online version of this book.)

on the thread's sensitivity. In order to examine the gauge factor as a function of twist angle, an analysis of variance (ANOVA) was performed on several threads of various twist angles with similar diameters as seen in Fig. 24.17. From the figure, it can be seen that lower twist angles have higher sensitivities, and it is believed that this higher sensitivity comes from the thread's overall resistivity being lower at lower twist angles (see Fig. 24.17). This lower resistivity in turn lowers the resistance, which then increases the gauge factor as defined in Eqn (24.1). Finally, it should be noted that this ANOVA analysis for resistivity vs twist angle was performed on the same thread's used for the ANOVA analysis for gauge factor vs twist angle [54]. It is believed that this lower resistivity at lower twist angles predominately comes from less tube interfacial interaction due to the higher tube alignment against the primary axis at lower twist angles. In summary, it appears that the sensitivity of the CNT thread can be enhanced by lowering the overall resistance of the thread. Thus, it is hypothesized that postspinning densification and annealing may also increase the gauge factor by lowering the overall resistivity of the thread.

24.3.2 Hysteresis

The next sensor performance area examined was hysteresis. Like the above-mentioned sensitivity experiments, the Instron 5948 was utilized to provide a low-frequency triangle wave to the thread for some specified amount of cycles. For this particular analysis, a 0.1-Hz signal with just less than 1% strain amplitude was applied to an as-spun thread for 100 cycles. Typical time history responses for this test along with hysteresis plots for stress–strain and resistance–strain can be seen in Fig. 24.18. From the figures, it can be seen that the stress–strain curve demonstrates consistent hysteresis, yet the resistance–strain curve does not appear to have any hysteresis characteristics. Instead, the resistance time history has a significant amount of drift, which will be discussed later in Section 24.3.4. This observed hysteresis behavior in the stress–strain curve is damping, and more analysis on this topic can be seen later in the Section 24.5.

From these 100 cycles, a representative single resistance–strain cycle from a particular test can be seen in Fig. 24.19 along with some statistics for the given test. As mentioned earlier, the thread went through 100 strain cycles. Each of these cycles was examined individually. Thus 100 averages were done for the analysis below.

From the figure, it can be seen that the loading and unloading curves generally follow the same pathway with minimal disagreement. However, this disagreement was quantified by integrating each loading and unloading curve at zero mean and then subtracting the instantaneous difference. The average and standard deviation of this loading, unloading, and difference integration can be seen in the Figure 24.19b. As seen in the table, the loading and unloading integrations were very close in magnitude and error, but this error was fairly high. The difference in loading was small, about 2–4% of the loading and unloading integral.Yet, the variance in this calculation was also high. Consequently, it appears that the CNT thread has the potential to have very low hysteresis (2–4%), but the high variance must be

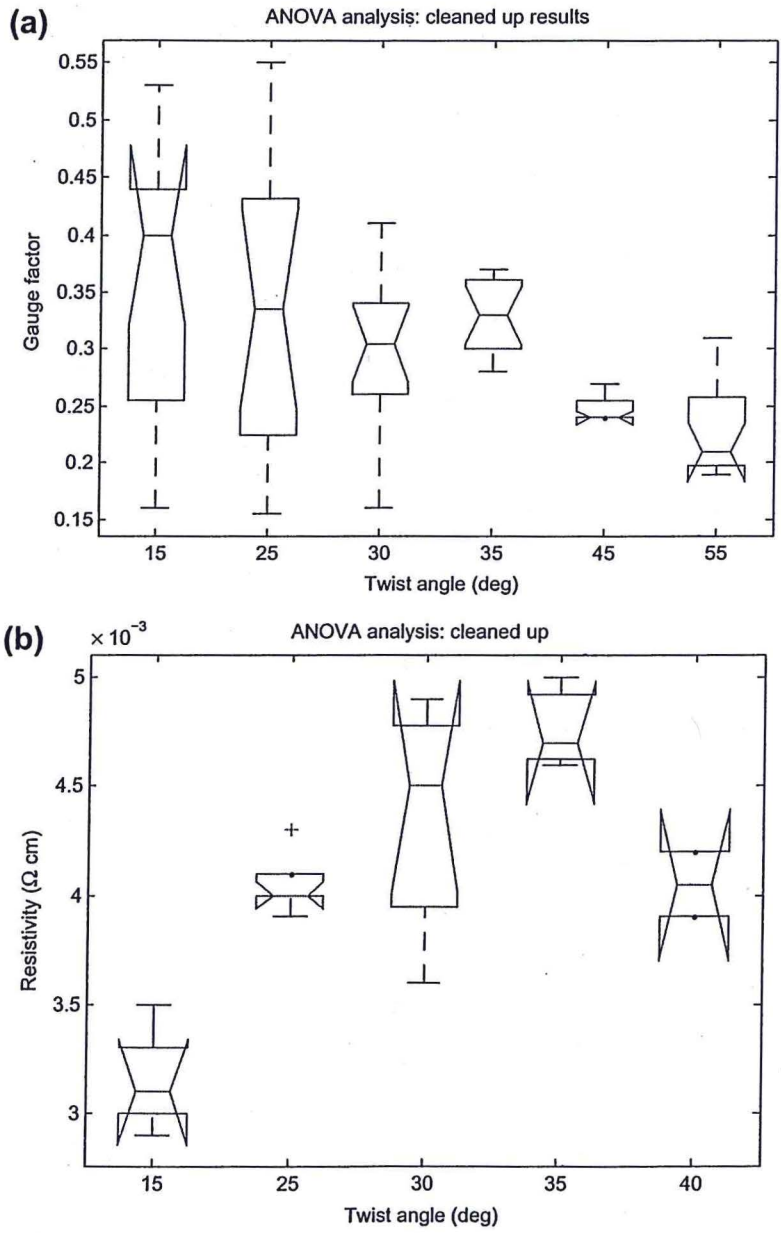

FIGURE 24.17

ANOVA analysis for CNT thread gauge factor optimization with twist angle. (a) ANOVA for CNT thread gauge factor as a function of twist angle. (b) Similar ANOVA was done for CNT thread resistivity as a function of twist angle. Note how the lower resistivity at lower twist angles contributes to a larger gauge factor at lower twist angles. These two analyses were done with 11 CNT threads of various twist angles made in Nanoworld Laboratories [54]. (For color version of this figure, the reader is referred to the online version of this book.)

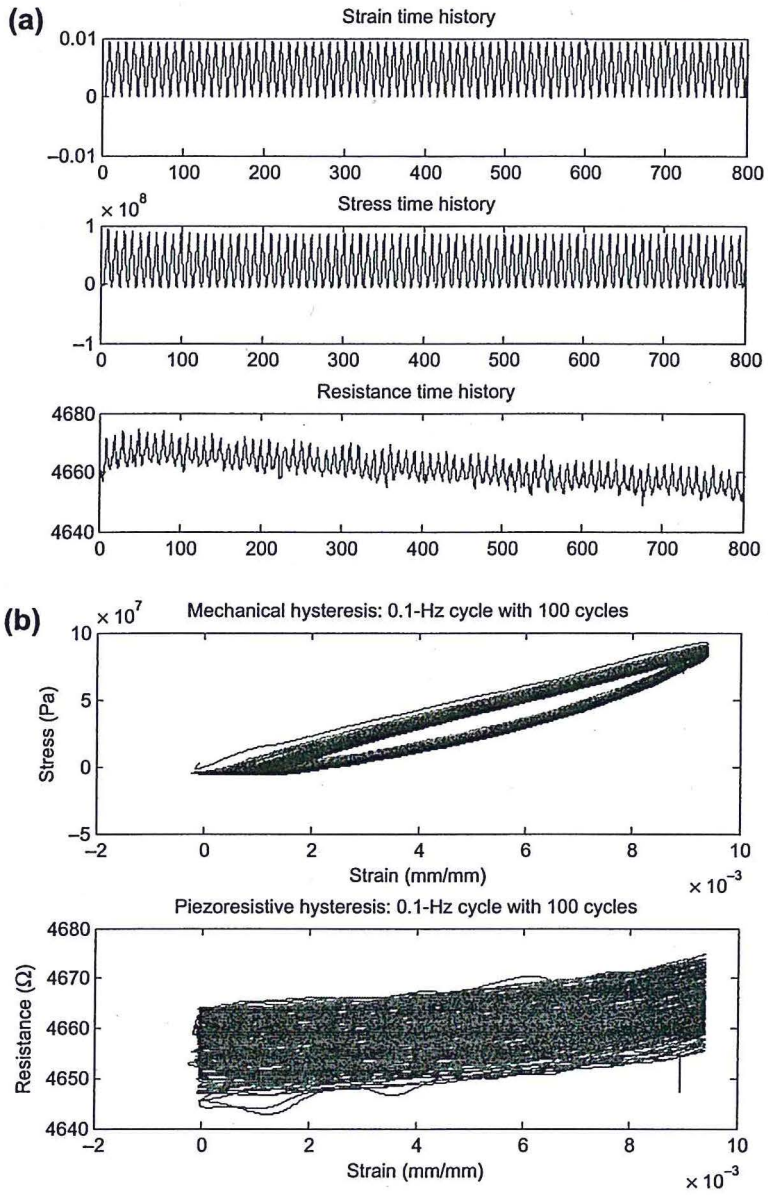

FIGURE 24.18

Hysteresis analysis of CNT thread. (a) Time histories of strain, stress, and resistance of the CNT thread during a typical hysteresis test and (b) time histories of stress and resistance plotted against strain to show consistency and correlations with consecutive strain cycles. Note that the hysteresis loop seen in the mechanical hysteresis plot implies damping. This will be discussed in more detail later. (For color version of this figure, the reader is referred to the online version of this book.)

(a)

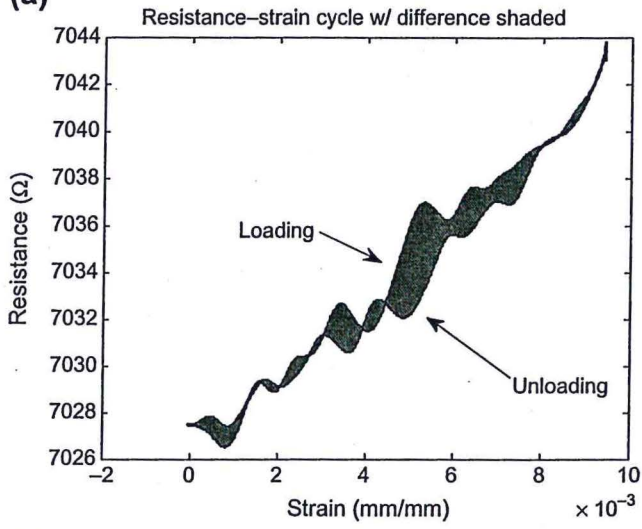

(b)

Piezo resistance hysteresis			
	Loading	Unloading	Difference in loading
Average (Ohm*mm/mm)	0.0514	0.0496	0.0018
Std (Ohm*mm/mm)	0.0133	0.0137	0.0107
% Std	25.88	27.62	N/A

FIGURE 24.19

Hysteresis behavior with statistics. (a) A single resistance–strain cycle for a given hysteresis test. As seen in the plot, the loading and unloading curves generally follow the same given path. (b) Statistics for 100 cycles, or 100 averages. The statistics represent how close the loading and unloading curves are by integrating under the curve without any DC offset (starting value of zero). The two curves are very similar in their average area, showing low hysteresis. (For color version of this figure, the reader is referred to the online version of this book.)

addressed. It is believed that this high variance is predominately from a poor signal to noise ratio (this measurement was done with four-wire approach) combined with temperature variations in the room. More will be discussed on these temperature variations in the Section 24.3.4.

24.3.3 Consistency

Consistency of the CNT thread strain sensor was analyzed by examining the consistency of the gauge factor of the thread after consecutive cycles. Thus, the gauge

Table 24.1 Gauge Factor Consistency

Gauge Factor Consistency			
	GF Loading	**GF Unloading**	**GF Cycle**
Average	0.226	0.219	0.222
Standard Deviation	0.0337	0.0373	0.0258
% Standard Deviation	14.91	17.03	11.62

This table shows how close 100 loading, unloading, and cycle point clouds are in their linear fit for the gauge factor. All the line fits are very close, which implies that the thread consistently measures the same change in resistance.

factor was calculated for each cycle of hysteresis curve above. In order to see how consistent the sensor was in loading, unloading, and the full cycle, a line was fit to each of these datasets. In other words, the loading and unloading curves seen in Fig. 24.19 each had a line fit to their trend. Then, a line was fit to the entire cycle (both curves' data points). The results for these line fits are tabulated in Table 24.1, and it should be noted that all line fits are very consistent and that the error is not excessively high. However, similar to the hysteresis analysis, this error is believed to be caused by a poor signal to noise ratio along with slight changes in room temperature. Nonetheless, it appears that CNT thread is indeed consistent in its sensitivity.

24.3.4 Stability

As mentioned earlier, drift in the CNT thread resistance measurement is fairly significant. To quantify the severity of this drift, the resistance values at 0%, 0.47%, and 0.94% strain were analyzed for a typical hysteresis test. Figure 24.20 below illustrates the points analyzed on the hysteresis curve with corresponding resistance values in (b). From the table, a net change of around 13 Ω is consistently measured, but the standard deviation is near 3 Ω. Additionally, this test takes about 15 min to complete, thus resistance values were not measured for a long period. As a result, two resistance measurements of the CNT thread at zero strain over a long period were made. This measurement was made with the bridge circuit seen earlier in Fig. 24.13 with the CNT thread balanced against standard resistors. It was found that the resistance did not stay very stable, in fact the standard deviation increased with time. These measurements can be seen in Fig. 24.21 with the blue and red curves.

These large variations in the resistance values seen in Fig. 24.21 are suspected to come from temperature variations in the testing room. From the two curves, sharp responses can be observed that may correlate to when the air-conditioning was turned on in the laboratory. As a consequence of the thread appearing to be

(a)

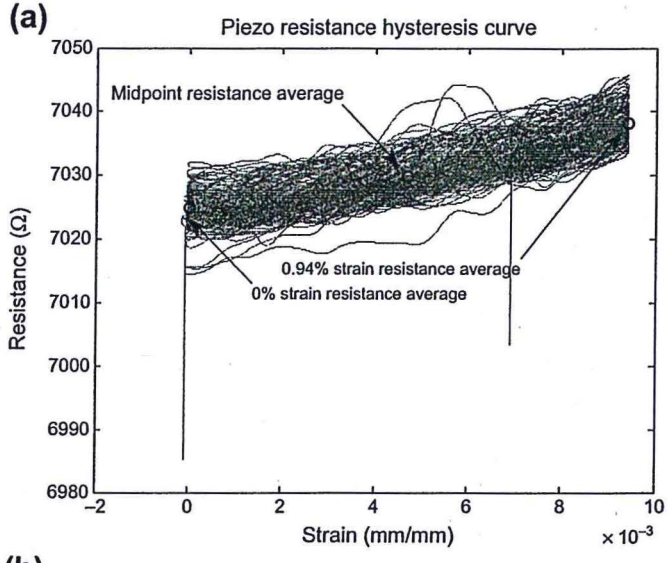

(b)

	Stability at close points, resistance values			
Strain	0%	0.94%	0.47% Up	0.47% Down
Average (Ω)	7024.9	7038.3	7029.5	7029.8
Std (Ω)	2.61	2.8	2.67	2.88
Std %	0.037	0.040	0.038	0.041

FIGURE 24.20

Resistance stability during strain cycles with statistics. (a) Illustration of CNT thread resistance response drift seen during a typical hysteresis test along with points of concern for analysis. These points are 0%, 0.47%, and 0.94% strain. (b) Statistics for a 100 cycle hysteresis test can be seen in the table. As seen from the table, the standard deviation at a particular strain is low relative to the average, yet the net change is not large enough to say that this deviation is insignificant. (For color version of this figure, the reader is referred to the online version of this book.)

extremely sensitive to temperature, another resistance measurement was made, yet with the CNT thread balanced against another CNT thread to separate out thermal effects. This measurement can also be seen in Fig. 24.21 as the black curve. This approach works because each thread should undergo a very similar change in resistance from temperature, which, in turn, would make the resistance measurement much more stable.

As a consequence of CNT thread being extremely susceptible to temperature variations, a reference thread may need to be embedded into the composite material, which does not undergo strain. This architecture would be difficult to accomplish, but may be possible. However, it should also be noted that once the CNT thread

(a)

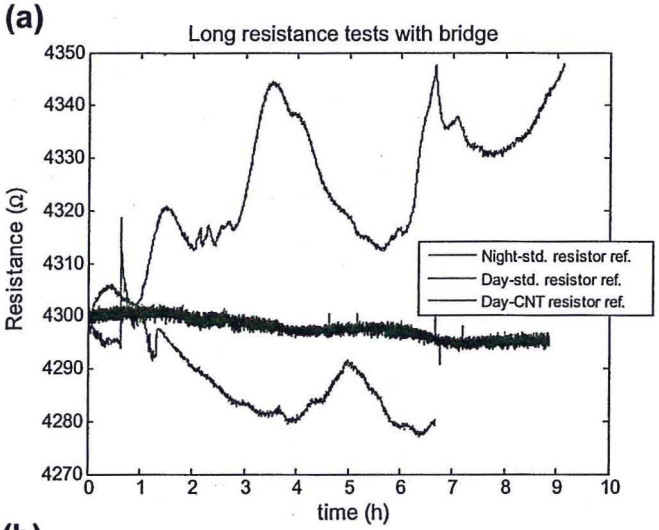

(b)

Reference resistor	Standard	Standard	CNT thread
Time of day	Afternoon–night	Night–morn	Morn–afternoon
Test time (h)	6.66	9.13	8.85
Mean (Ω)	4287.6	4324.4	4297.8
Std. dev (Ω)	6.93	12.65	1.97
Max (Ω)	4318.9	4348	4302.1
Max (Ω)	4277.2	4295.9	4290.7
Max min diff (Ω)	41.7	52.1	11.4

FIGURE 24.21

Resistance stability under no strain for long periods with statistics. (a) CNT thread resistance from a Wheatstone bridge circuit for a long time. The blue and red curves (standard ceramic resistance balance resistor) tend to drift and undergo low-frequency oscillations due to suspected temperature changes in the room (air-conditioned system). The black curve on the other hand does not undergo these dramatic drifts, but remains fairly stable due to the CNT thread being balanced another CNT thread that undergoes similar thermal effects. (b) Key comparison statistics from these three curves. (For interpretation of the references to color in this figure legend, the reader is referred to the online version of this book.)

is embedded into the composite material, the thermal mass of the material will be much larger, which will minimize temperature variations that the thread would experience compared to the thread in open air. Thus, embedded thread may be much more stable.

24.3.5 Bandwidth

The final performance criterion under investigation is the strain bandwidth of the thread. In order to approximate the thread's bandwidth, a calibration measurement was made against a reference strain gauge calibrated from 0 to 1600 Hz. This particular range was chosen because the thread is planned to be embedded into large composite structures. Also, a high bandwidth is needed to detect impact events. These large composite structures typically have many fundamental modes (natural frequencies) of vibration below 10 Hz, yet an impact could be much higher in frequency (100–10,000 Hz). Thus, to be an effective dynamic structural health and strain sensor, these frequency ranges must be measured.

In order to perform this calibration, (1) the sensor must undergo significant strain to cause a measurable resistance response in the thread and (2) the various frequencies of concern must undergo measurable strain. In other words, the structure should have a somewhat broadband response and not many antimodes. In order to achieve these goals, a custom double-cantilever calibration rig made out of aluminum was designed and built. This calibration rig was then mounted to an electromagnetic shaker for excitation. The initial design geometries of this structure were chosen so that there would be large strains and many modes of vibration within the spectrum of concern. This calibration rig can be seen in Fig. 24.22 in its naked form along with sensors mounted to the structure for the calibration measurement. It should be noted

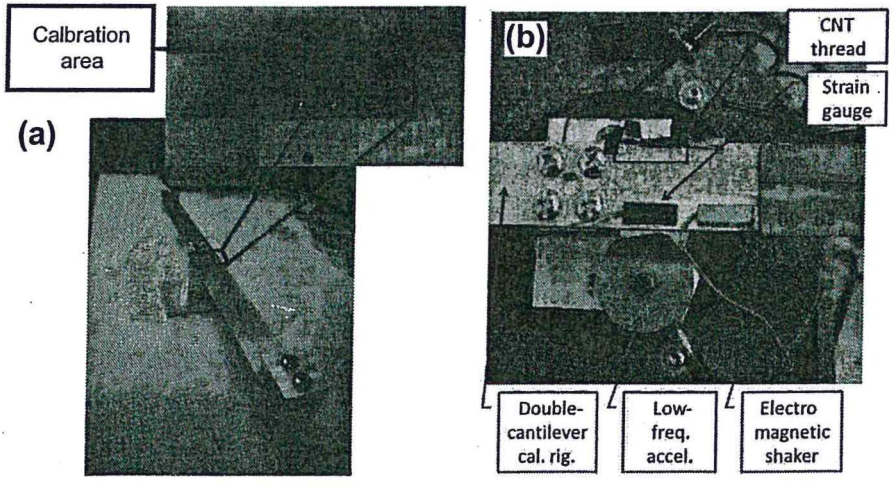

FIGURE 24.22

Custom double-cantilever beam strain calibration rig for CNT thread strain sensor. (a) Custom-built strain calibration rig in its naked form with calibration area highlighted. (b) Calibration area with the thread mounted adjacent to the reference strain gauge. It should be noted that this thread is close to 20 μm in diameter and about 12.5 mm in length. (For color version of this figure, the reader is referred to the online version of this book.)

that the sensors that were used to make this calibration were piezoelectric strain gauges (PCB Piezotronics Inc 740A02 and 740M04), which are calibrated from 0.5 Hz–100 KHz, and a piezoelectric accelerometer (PCB Piezotronics Inc 301A11), which is calibrated from 0.5 Hz–10 KHz. The electromagnetic shaker is an MB-50 and an HP 45670A frequency analyzer was used for the presented measurements.

The thread in the above photograph is mounted close to the surface of the aluminum beam with two epoxy mounting points. It should be highlighted that the thread was not entirely encased in epoxy in order to obtain a baseline measurement prior to infiltrating the entire thread with epoxy. This thread mount is not a true strain measurement of the beam because the thread does not conform to the surface of the beam. Instead, it is a displacement measurement of two points. This technique was acceptable here because the thread was nearly the same size as the strain gauge, so this mounting technique proved not to be a problem. After the epoxy mount points, conductive epoxy was utilized to hook up small wires. The thread could then be hooked up with the Wheatstone bridge circuit seen in Fig. 24.13. A detailed schematic of this mounting configuration can be seen in Fig. 24.23. Finally, it should be noted that this mounting technique may prove to be beneficial in certain sensing applications for strain amplification or separation.

Prior to performing any frequency domain analysis, the CNT thread response time history quality was analyzed. This was done by exciting the calibration rig near resonance with a 35 Hz sine wave while measuring the voltage output from the Wheatstone bridge. This voltage or thread response along with the response of the other sensors used in this experiment can be seen in Fig. 24.24. As seen below,

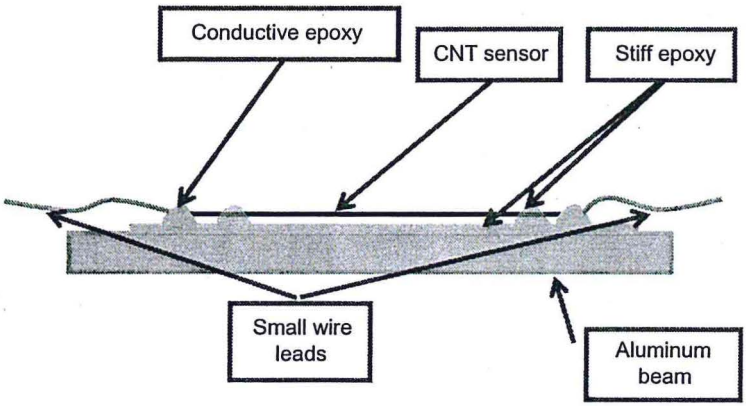

FIGURE 24.23

CNT thread attachment to aluminum calibration rig. As seen in the schematic, drops of epoxy are utilized to keep the thread in tension once mounted, conductive epoxy is used to hook up lead wires, and the thread is mounted above a surface of thin epoxy to ensure electrical insulation and to avoid uneven surfaces. (For color version of this figure, the reader is referred to the online version of this book.)

the CNT thread has a "clean" sine wave output, which is desired for optimal frequency response function (FRF) estimation. This clean signal was obtained by pretensioning the CNT thread during mounting. Thus, when the beam goes into compression, the thread does not go slack. In summary, this test was performed to ensure that the thread would not go slack during testing so that FRF estimation could take place.

After a clean sine wave was obtained near peak excitation, FRFs were generated to (1) determine the bandwidth of the thread and (2) calibrate the thread against the reference strain gauge. An FRF is defined as the output parameter over the input parameter across several frequencies of concern as defined below in Eqn (24.3) for the frequency domain. This function provides a description of how the output's response varies over various frequencies relative to an input, thus system behavior can quickly and easily be understood by measuring this function.

$$\mathrm{FRF}(\omega) = \frac{\mathrm{Output}(\omega)}{\mathrm{Input}(\omega)} \tag{24.3}$$

To generate FRFs, an excitation technique must be utilized, which puts known frequencies into the system. In its simplest form, this would be a periodic sine wave. However, sine wave excitation is very time consuming, frequency resolution would not be the best, averaging could not be done as easily, and a somewhat larger amplitude signal is needed to visually see the signal. To handle these disadvantages, a chirp excitation (quick periodic sine wave sweep) was utilized combined with 50–100 root mean square averages of various frequency resolutions to estimate FRFs in this chapter. This estimation process for the calibration rig's base acceleration and strain can be seen in Fig. 24.25 as an example. It should be pointed out that the FRFs in this chapter are also plotted with the ordinary coherence function to quantify the quality of the FRF estimate. A coherence of 1 implies good correlation or measurement quality.

One of the first analyses of this system can be seen in Fig. 24.26 comparing FRFs of CNT thread to base acceleration and strain gauge to base acceleration. As seen in the figure, this analysis provided a conservative bandwidth estimate of the thread, which ranged from 0 to 350 Hz. It should be noted that this bandwidth measurement is conservative because the mounting epoxy damps the strain that the CNT thread experiences and limits the received energy. Thus, it is expected that higher bandwidths could be achieved with stiffer epoxy. Nonetheless, stiffer epoxies will still limit the bandwidth of the thread and ultimately the sensing once embedded into composites. Despite this low bandwidth, this frequency range meets the prior requirements of measuring structural modes and detecting lower frequency impacts.

After the CNT thread bandwidth was determined for this setup, a 0–100 Hz FRF was made between the CNT thread and adjacent strain gauge originally seen in Fig. 24.22. This lower frequency range was selected because (1) predetermined rig dynamics showed that this range was best for calibrating the thread and (2) thread response cuts off shortly thereafter. This measurement can be seen in Fig. 24.27. As seen below, coherence is decent in the range of interest except at lower frequencies. It

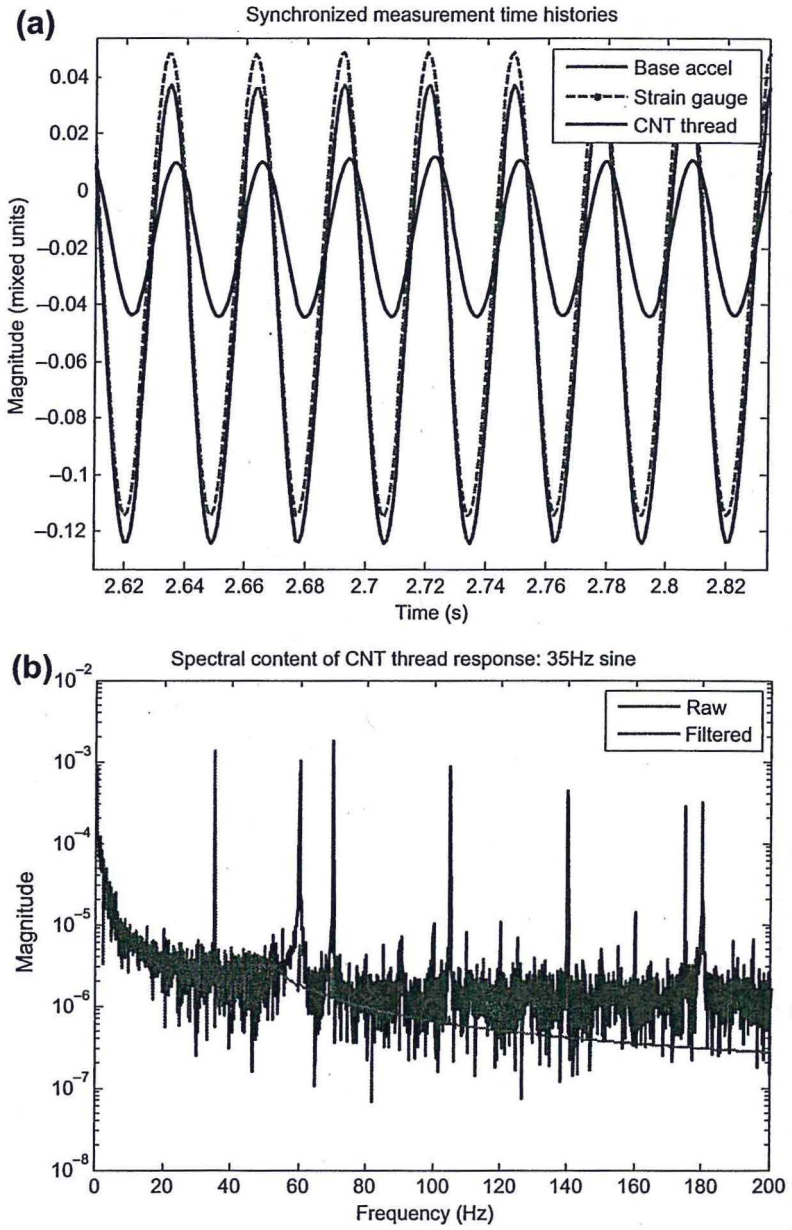

FIGURE 24.24

Sine wave of CNT thread to 35-Hz resonance excitation. Prior to performing frequency domain analysis, the CNT thread was confirmed to have a "clean" sine wave appearance. In order to obtain this clean signal, the thread's output was filtered with a tight low-pass filter.

is believed that this drop comes from low input energy combined with potential standing waves setting up on the thread. Yet, when the coherence improves, the FRF appears "flat" and the phase angle is near zero, as expected. This flatness and near-zero response is expected because the thread is nearly the same size as the reference strain gauge and measures nearly the same strain state on the opposite side of the beam. Thus, calibration can be done to determine the gauge factor within this range, or the gauge factor FRF of the thread can be calculated. This calibration is still being performed.

In summary, this analysis shows that (1) CNT thread can measure frequencies of interest, specifically structural modes and impacts, and (2) the CNT thread can be calibrated against a reference strain gauge to estimate sensitivity or gauge factor over multiple frequencies. This work would not have been possible without the advisement and generosity of the Structural Dynamics Research Lab here at UC.

24.4 CARBON NANOTUBE THREAD SHM ARCHITECTURES

Developing an SHM sensor for composite materials or a structure is only part of the SHM solution. How this sensor will be incorporated into the structure, how many sensors should be used, and how the sensor data will be used are all other important areas that also need to be addressed for a holistic SHM approach. This section will briefly address some of these questions.

On a few previous occasions, it has been mentioned that the CNT thread sensor can detect specific damage modes such as ply delamination and matrix cracking. Matrix cracking can occur from several different mechanisms itself, and it would be advantageous to know which mechanism is the culprit of the cracking. It is believed that the CNT sensor thread can shed light on some of these cracking mechanisms by (1) confidently identifying a crack in the structure and (2) utilizing neighboring thread sensors to help assess what particular mechanism is at play for better health and repair assessments. The sensor thread can be seen in Fig. 24.28 identifying these various cracking mechanisms of concern.

In order to assess the mechanism behind cracking or identifying other damage modes, the sensing thread needs to have a minimum density and a clever incorporation design in order to identify damage in its nascent stages. This incorporation design should provide information about damage location, severity, and potential prognosis in addition to damage mode characterization. One design that would meet these criteria and be easy to incorporate into current composite materials is a cross-weave or grid design. This design can be seen in Fig. 24.29

(a) Clean sine wave time history along with outputs from the strain gauge and accelerometer and (b) frequency domain of CNT thread signal before and after filtering. It should be noted that the thread's output was on the same order as 60-Hz noise. Other peaks in the spectrum are harmonics of this 35-Hz excitation and of the 60-Hz noise. (For color version of this figure, the reader is referred to the online version of this book.)

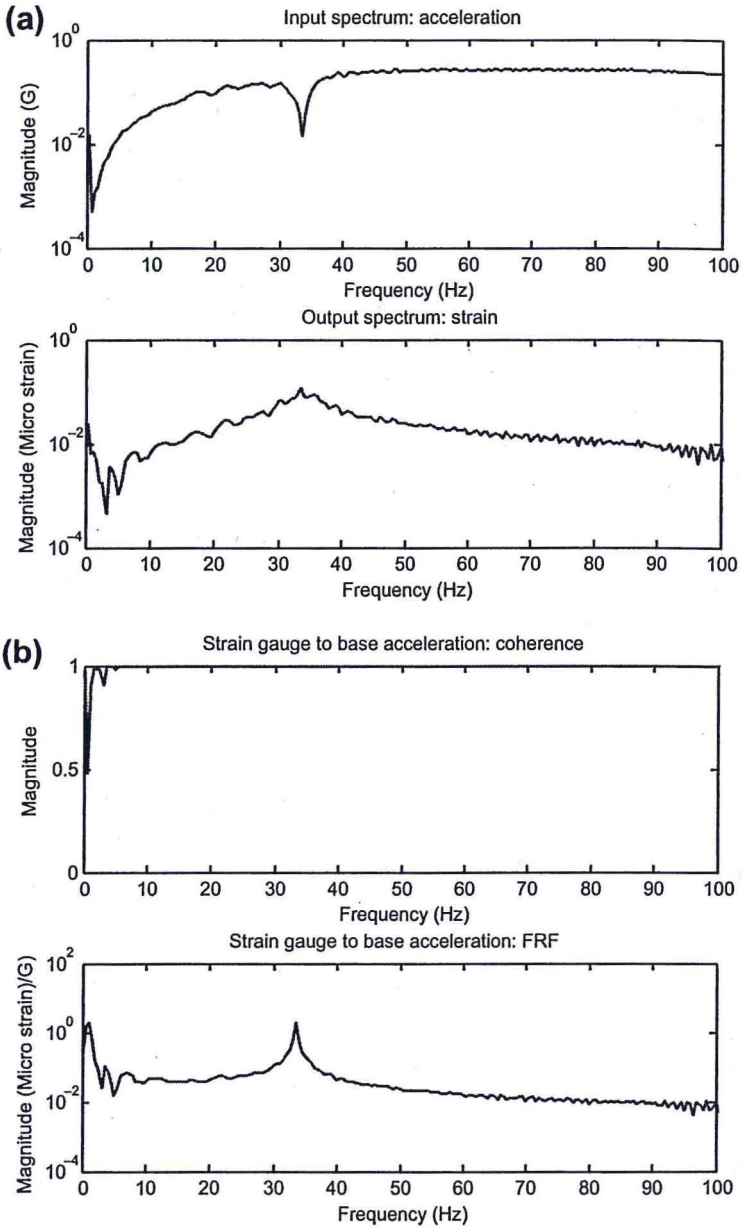

FIGURE 24.25

Frequency domain analysis and frequency response function (FRF) estimation. (a) Linear input spectrum from the base acceleration and output spectrum from the strain gauge. As seen from the plot, the electromagnetic shaker struggles to put low-frequency energy into the system, while the strain gauge spectrum shows a rise near the beam's first resonance. These spectrums can then be used to estimate the FRF of the system. (b) FRF of the system with ordinary coherence. Ordinary coherence is a statistical tool used to ensure/determine FRF quality. (For color version of this figure, the reader is referred to the online version of this book.)

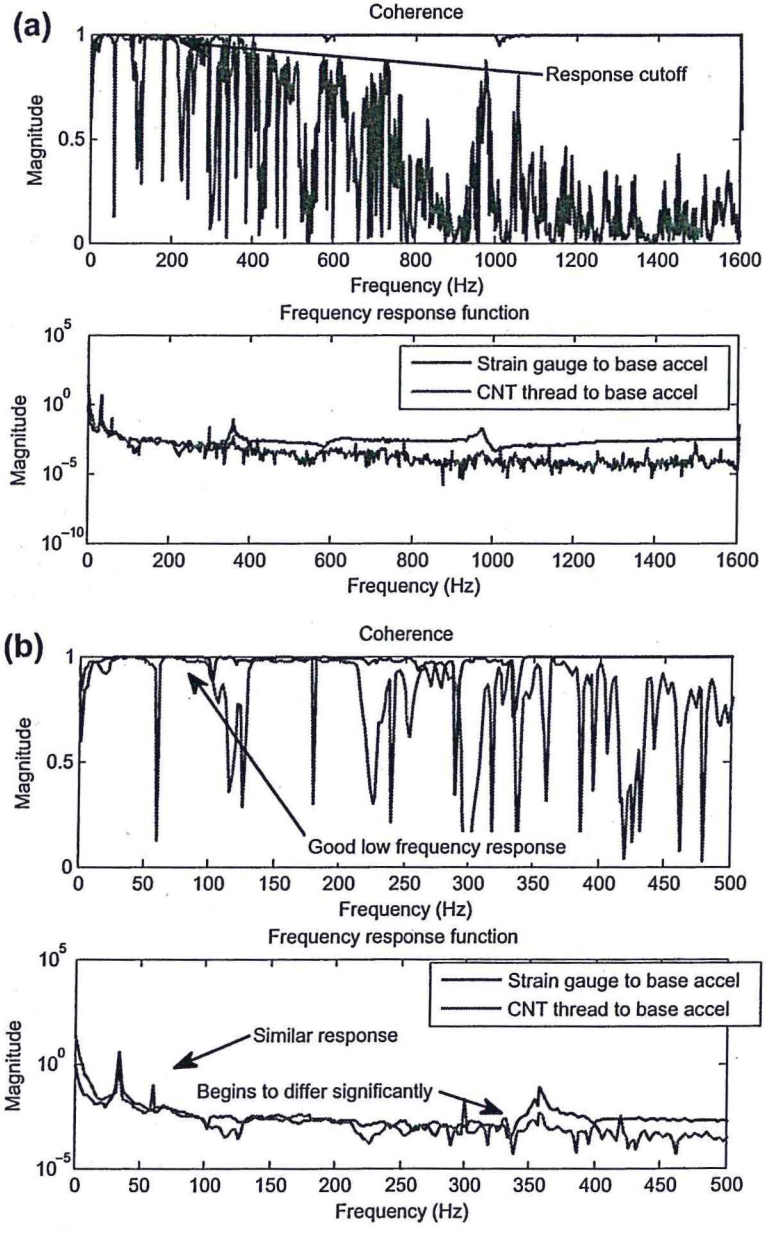

FIGURE 24.26

The 0–1600 Hz FRF of strain gauge and CNT thread to base acceleration. (a) Strain gauge and CNT thread from 0 to 1600 Hz. As seen in the coherence, the output response begins to diminish at higher frequencies. (b) Zoomed in region of the coherence and FRF where this poor response begins to happen. As pointed out in the figure, it seems like the FRFs between the two sensors diverge near 300–350 Hz. (For color version of this figure, the reader is referred to the online version of this book.)

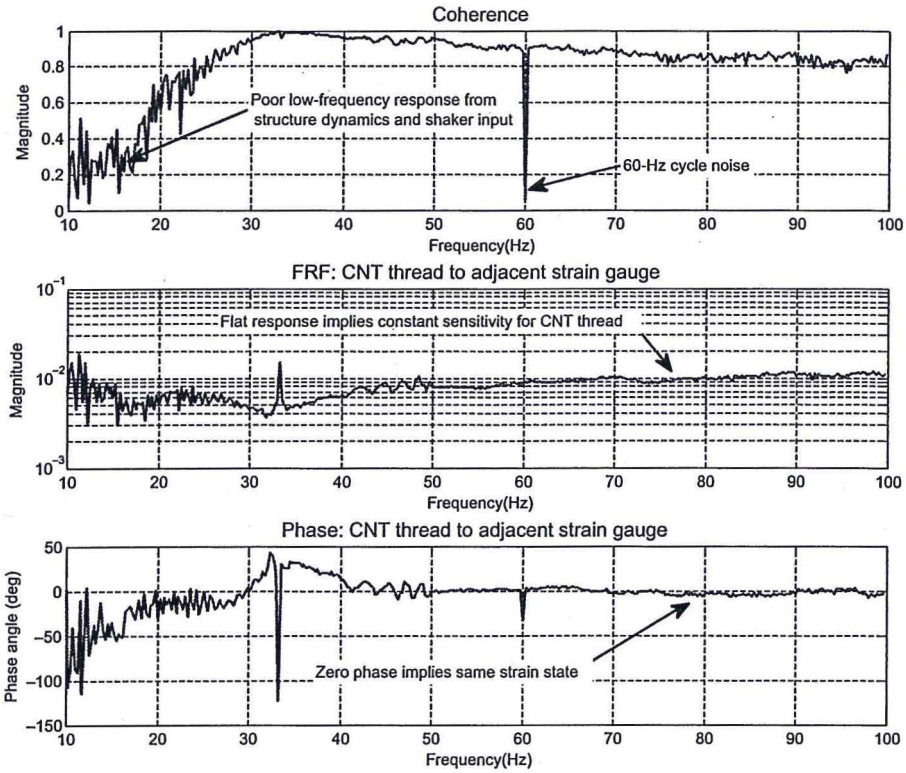

FIGURE 24.27

The 10- to100-Hz FRF of CNT thread to strain gauge. This figure illustrates how the CNT thread can be used as a broadband sensor due to its near-constant sensitivity (flatness) and near-zero phase angle. This FRF can be scaled with calibration values from the strain gauge and Wheatstone bridge circuit to construct a gauge factor FRF. This calibration is still being carried out. (For color version of this figure, the reader is referred to the online version of this book.)

with a potential sensor thread incorporation scheme during the fabrication of the material. Additionally, this fabrication method would easily allow various thread densities for optimal damage identification. As seen in the figure, this design would also utilize multiplexing switches for data channel reduction combined with an algorithm to analyze CNT sensor signals for damage location, severity, and characterization.

Multiplexing will be done in the time domain by pulsing and assessing each sensing thread in close vicinity. Close vicinity monitoring will be implemented to simplify data handling by utilizing sensing nodes to do localized data processing. These sensing nodes will then utilize wireless transmitters to send limited yet meaningful health assessment information to the operator of the aircraft. A simplified

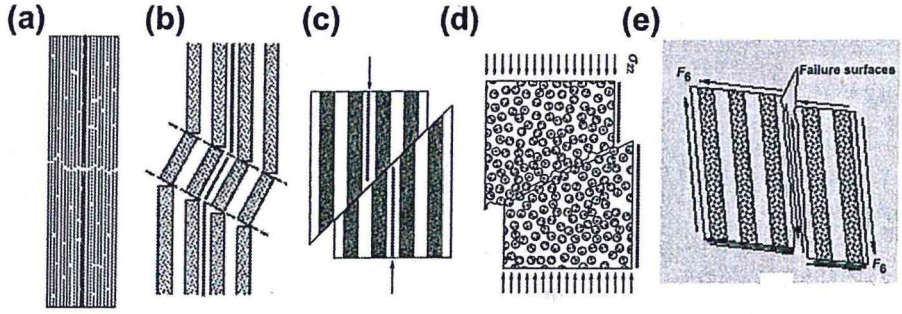

FIGURE 24.28

Micromechanical failure modes in laminated composites. (a) Coalescing of microcracks in a composite subjected to tensile loading in the fiber direction. (b) Failure of a composite with brittle fibers subjected to compression in the direction of the fibers. (c) Shear failure in a composite with a high fiber volume fraction loading in the transverse direction to the fiber. (d) Shear failure in a composite subjected to compression loading in the transverse direction to the fiber. (e) Shear failure in a composite subjected to in-plane shear loading. (For color version of this figure, the reader is referred to the online version of this book.)

Source: All images edited from[55] by Jandro Abot and M. Schulz.

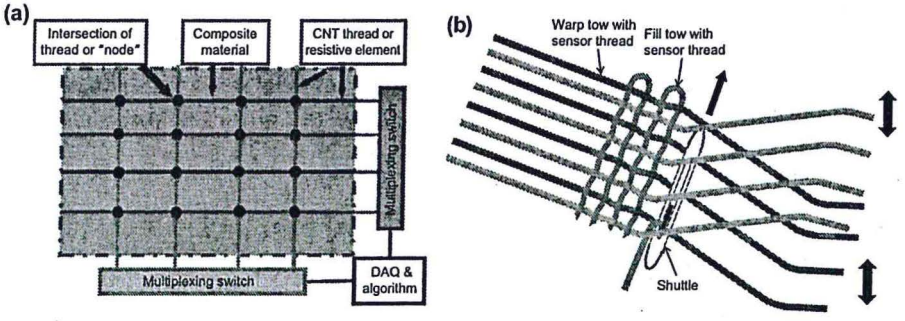

FIGURE 24.29

Array configuration of sensors. (a) Spatial grid design for detailed failure information and (b) industrial scale-up manufacturing process for prepreg plain weave fabrics. (For color version of this figure, the reader is referred to the online version of this book.)

representation of this proposed multiplexed and distributed sensing node design can be seen in Fig. 24.30.

To illustrate how this SHM architecture would be used in a specific application, the F-22 Raptor [57] is used as a design example, as seen in Fig. 24.31, with detailed areas of concern. It should be noted that the F-22 is built by several manufacturers. Boeing takes care of building the aft fuselage, main wings, power supplies, auxiliary power units, auxiliary power generation systems, airframe-mounted accessory drives and the fire-protection system. The aft fuselage is 67% titanium, 22% aluminum and

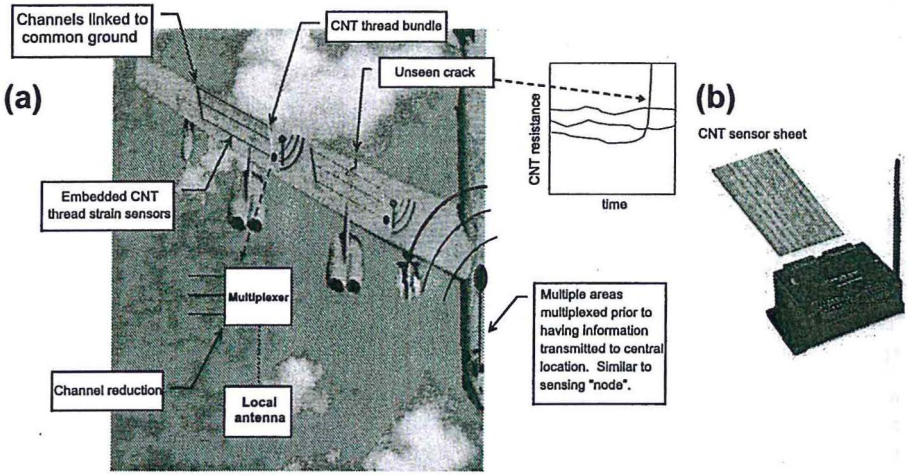

FIGURE 24.30

SHM system communication. (a) CNT thread strain/damage sensor wired multiplexer, local antenna. (b) Off-the-shelf multiplexer and wireless transmitter [56]. (For color version of this figure, the reader is referred to the online version of this book.)

11% composite by weight. The Boeing-built portion of the wing is 42% titanium, 35% composite and 23% aluminum; steel and other materials are present in the form of fasteners, clips and other miscellaneous parts, also by weight. Each wing weighs about 2000 pounds. Titanium reinforcement was added for strength against impact during combat. Nonetheless, most ribs and spars in the wing are composites and it would be beneficial to actively monitor their health.

24.5 AREAS OF STRONG MULTIFUNCTIONAL POTENTIAL

Besides adding strain and damage sensing to a polymeric composite material, CNT thread has the potential to improve the material in other ways as well. In other words, the CNT thread would be multifunctional in how it would improve the overall performance and quality of the material. Some of the potential areas where CNT thread could have an impact on composite material improvement are listed in the introduction of this chapter, but only the areas of current investigation will be covered in this section, specifically damping and toughness.

As observed in earlier sensing hysteresis analysis (see Fig. 24.18), CNT thread exhibits significant hysteresis in the stress–strain curve. This hysteresis can be considered to be mechanical damping or mechanical energy loss since mechanical energy is not being conserved in the loading cycle. This damping can be quantified by finding the hysteresis loop area normalized by the maximum mechanical energy (U_{max}) as defined below in Eqn (24.4). This quantity, u, is called the specific

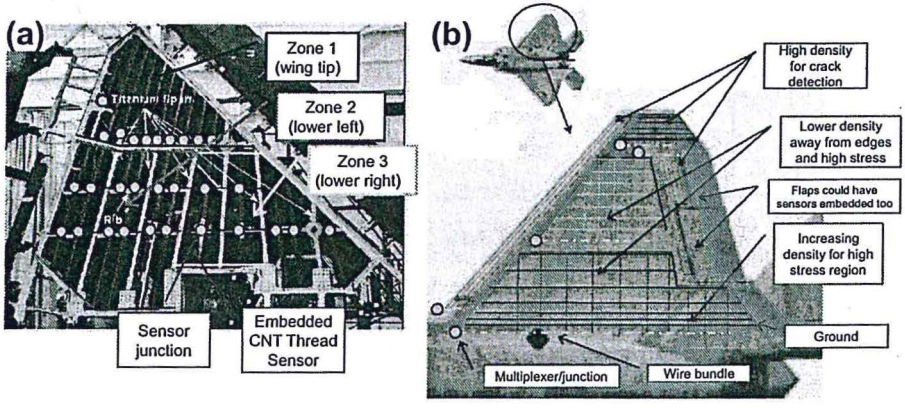

FIGURE 24.31

Example design of the SHM system for retrofit to an aircraft. (a) Sensor thread design for the F-22 interior wing with 29 junctions where sensor connects with multiplexed network; three multiplexers will be used to manage information from specific zones of wing, 39 spar sensor threads and 20 rib sensor threads, Close to 60 total sensors are needed. Each zone could transmit via antenna to central location. (b) Sensor thread design for the F-22 exterior wing with five multiplexers to manage information from specific zones of wing, four to five sensors in front wing edge (close spacing, 1–2″), four to five sensors around flaps (close spacing, 1–2″), 15 to 20 sensors in wing tip grid (dense, 3–5″ spacing), 15–20 sensors in midwing (low density, 8–10″), and 15–20 sensors in lower wing (high and low density, 3–5″ and 10–12″), around 100 total sensors. Each zone transmits wirelessly to the central location. (For color version of this figure, the reader is referred to the online version of this book.)

Source: Inner wing photo courtesy of DOT&E FY 2001 Report.

damping capacity [58], but it can also be thought of as an energy loss percentage. In order to implement this equation numerically, the damping capacity can be calculated by finding the difference of the integrated loading and unloading curves. Then, this quantity can be normalized by the loading curve. These curves are labeled in Fig. 24.32 for both as-spun CNT thread and copper wire. As seen in the figure, the materials were both strained in their elastic regions to approximate values of specific damping capacity. Copper wire was used not only for comparison purposes but also to ensure that the method of generating this hysteresis curve was valid and not an artifact of the Instron 5948's sensors/structure.

$$u = \frac{(\oint \sigma d\varepsilon)}{U_{\max}} = \frac{\left(\int_0^{\varepsilon_{\max}} \sigma_{\text{loading}} d\varepsilon - \int_0^{\varepsilon_{\max}} \sigma_{\text{unloading}} d\varepsilon\right)}{\int_0^{\varepsilon_{\max}} \sigma_{\text{loading}} d\varepsilon} \tag{24.4}$$

Once the specific damping capacity is found, the loss factor, or specific damping capacity per unit radian can be found as defined below in Eqn (24.5) [58]. Typically,

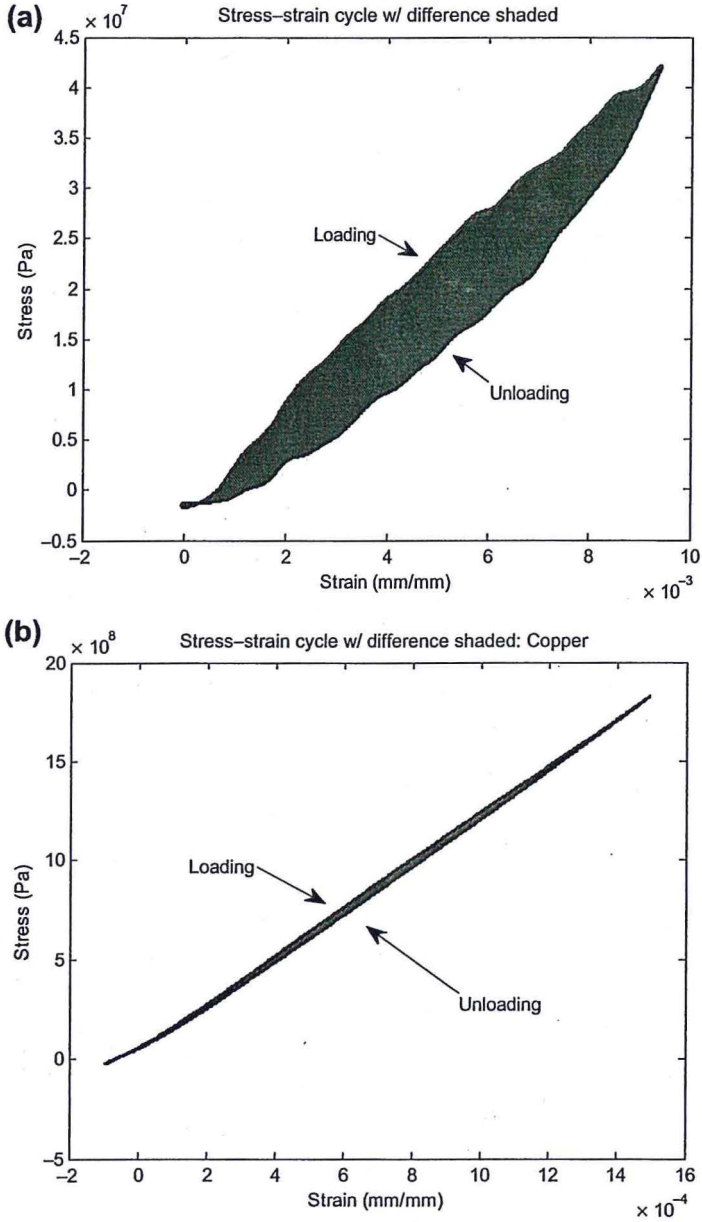

FIGURE 24.32

Energy dissipation through damping generated with Instron 5948. (a) As-spun CNT thread energy loss and (b) copper wire energy loss. The shaded region for the CNT thread is around 30% energy loss and around 3% for the copper wire. (For color version of this figure, the reader is referred to the online version of this book.)

materials are compared with their loss factor or damping ratio. If the loss factor is small, the damping ratio can be approximated by multiplying the loss factor by two. Figure 24.33 compares the loss factors of CNT thread, epoxy, rubber, aluminum, and glass.

$$\text{Loss Factor} = \frac{u}{2\pi} \tag{24.5}$$

As seen in the figure above, the CNT thread is close in magnitude to epoxy resin. It can then be inferred that if CNT thread were to be embedded into a polymeric composite material with an epoxy matrix, the overall material damping will not degrade. Instead, the composite material will maintain or better the effective damping of the material. As a result, CNT thread has the potential to improve composite material damping.

Another strong multifunctional area of CNT thread is toughness or damage limiting. Toughness is defined as the area under the stress–strain curve as defined in Eqn (24.6) and seen in Fig. 24.34 for as-spun CNT thread. Current as-spun CNT thread produced in Nanoworld Laboratories has 100–200 MPa strength and 3–5% elongation. The epoxy resin has 55–130 MPa strength with 2–4% elongation [39]. Thus, the toughness of as-spun CNT thread is on the order of that of epoxy

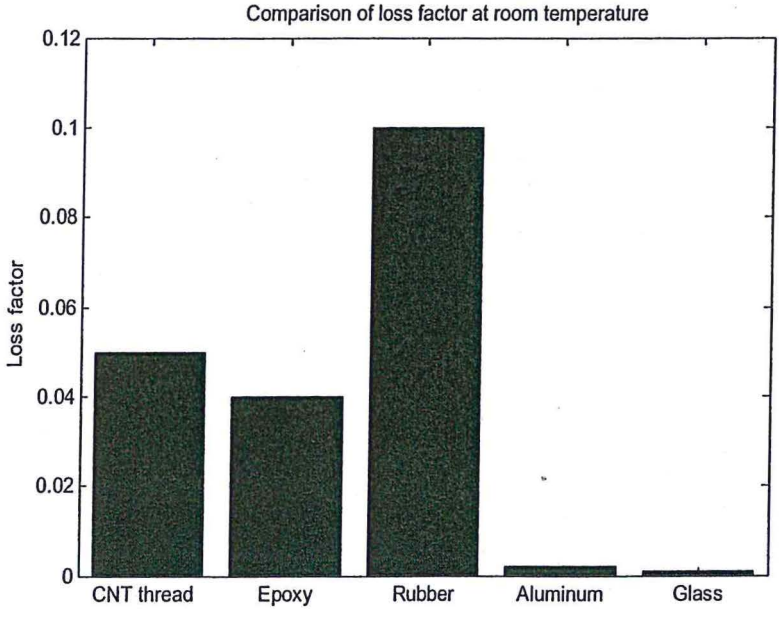

FIGURE 24.33

Loss factor comparison. Calculated CNT thread loss factor is compared against published values for epoxy [59], rubber, aluminum, and glass [58]. (For color version of this figure, the reader is referred to the online version of this book.)

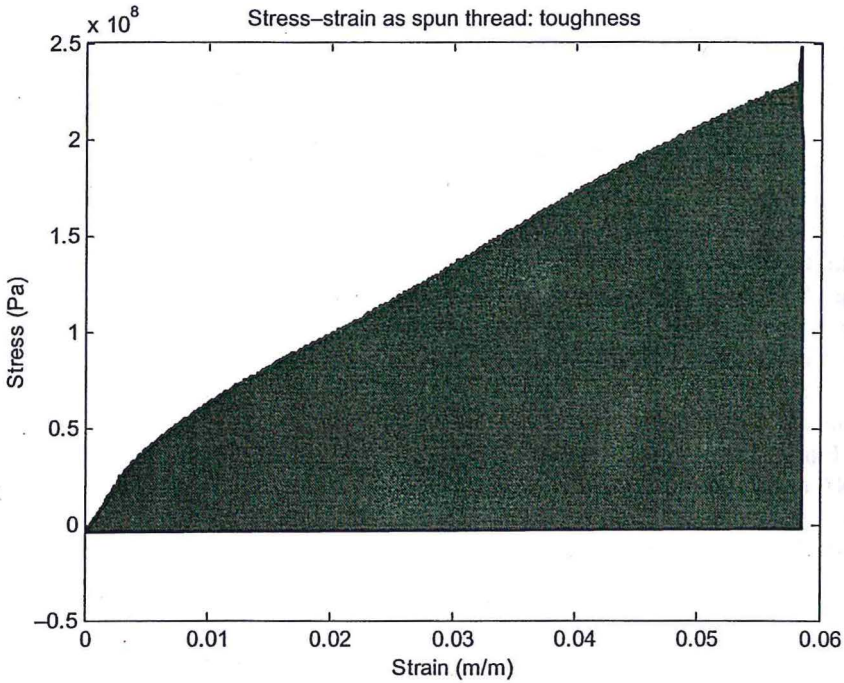

FIGURE 24.34

Stress–strain curve of CNT thread with area under the curve shaded, which represents material toughness. (For color version of this figure, the reader is referred to the online version of this book.)

resin. It can then be inferred that CNT thread has the potential to improve material toughness, which increases the material's resilience to damage.

$$\text{Toughness} = \int_0^{\varepsilon_{break}} \sigma d\varepsilon \tag{24.6}$$

24.6 FUTURE WORK

Future CNT thread sensor work at Nanoworld Laboratories entails several key areas of investigation to prove sensor feasibility for a composite SHM sensor. These key areas of investigation are listed below with descriptive significance.

- Embedded sensor performance: Although CNT thread appears to perform well outside the composite material, it must have similar if not improved sensor performance once embedded into the material. This will be similar to earlier concept work presented in Section 24.2.

- Sensor invasiveness: It is suspected that the CNT thread sensor will be minimally invasive to the composite material due to its small size. However, this hypothesis will be tested by examining composite breaking strength, stiffness, elongation, and fatigue strength.
- Failure mode identification: Composite materials will be fabricated with voids and cracks. Then, the composite material will be excited with broadband excitation to identify these impregnated damage modes with the strain response of the thread. Additionally, impact testing will be done on the composite material to (1) identify the impact through the strain response and (2) potentially assess the damage through CNT thread breakage strain response.

Acknowledgments

First and foremost, the principal author would like to thank Dr Schulz and Dr Shanov, directors of Nanoworld Labs, for their support, suggestions, and excellent advisement. Next, the author would like to thank the National Science Foundation for their support, and this material is based on work supported by the National Science Foundation under Grant No. 1102690. The author would also like to thank Doug Hurd, manager of the machine shop at UC, for his advisement in test rig design and manufacturing. The author would also like to thank Wenyu Zhao, of the University of Cincinnati Center for Intelligence Maintenance Systems (http://www.imscenter.net/), for his generosity in borrowing an NI 9205 DAQ system long term. Finally, the author would like to thank Dr Allemang and Dr Phillips of the University of Cincinnati Structural Dynamics and Research Lab (SDRL, http://sdrl.uc.edu/) for their generosity for borrowing a shaker, sensors, an FRF analyzer, and laboratory space to perform the strain bandwidth work. These individuals also provided suggestions in design of the calibration rig, analysis techniques, and general suggestions. Their advisement is greatly appreciated.

References

[1] Federal Aviation Administration of the USA. AC 43-204 Visual Inspection of Aircraft, 1997.

[2] Federal Aviation Administration of the USA. AC 20-107B Composite Aircraft Structure, 2009.

[3] A. Kapadia, Non-Destructive Testing of Composite Materials, National Composites Network. http://www.compositesuk.co.uk/LinkClick.aspx?fileticket=14Rxzdzdkjw=&.

[4] File:LockheedMartin F-22A Raptor JSOH.jpg.Wikipedia. (Online) (Cited: November 15, 2012)] http://en.wikipedia.org/wiki/File:Lockheed_Martin_F-22A_Raptor_JSOH.jpg.

[5] File:AH-64D Apache Longbow.jpg. Wikipedia. (Online) (Cited: November 15, 2012) http://en.wikipedia.org/wiki/File:AH-64D_Apache_Longbow.jpg

[6] File:All Nippon Airways Boeing 787-8 Dreamliner JA801A OKJ.jpg. Wikipedia. (Online) (Cited, 2012 (Online) (Cited: November 15, 2012). http://commons.wikimedia.org/wiki/File:All_Nippon_Airways_Boeing_787−8_Dreamliner_JA801A_OKJ.jpg.

[7] J.W.C. Pang, I.P. Bond, A hollow fibre reinforced polymer composite encompassing self-healing and enhanced damage visibility, Composite Science and Technology 65 (11-12) (2005) 1791−1799.

[8] S. Sen, E. Schofield, J.S. O'Dell, L. Deka, S. Pillay, The development of a multi-functional composite material for use in human space exploration beyond low-earth orbit, JOM 61 (1) (2009) 23–31.

[9] K.L. Schaaf, Composite Materials with Integrated Embedded Sensing Networks, PhD Dissertation, UC San Diego (2008).

[10] J.R. Zayas, D.P. Roach, M.A. Rumsey, W.R. Allan, D.A. Horsley, Low-Cost Fiber Bragg Grating Interrogation System for in situ Assessment of Structures, SPIE, Sensors and Smart Structures Technologies for Civil, Mechanical, and Aerospace Systems, San Diego, CA, March 18th 2007.

[11] B.R. Loyola, K.J. Loh, V.L. Saponara, Static and dynamic strain monitoring of GFRP composites using carbon nanotube thin films, SPIE, Sensors and Smart Structures Technologies for Civil, Mechanical, and Aerospace Systems, San Diego, CA, March 2011.

[12] N.D. Alexopoulos, HYPERLINK " C. Bartholome, HYPERLINK "http://www.sciencedirect.com/science/article/pii/S0266353809003807" P. Poulin, HYPERLINK "http://www.sciencedirect.com/science/article/pii/S0266353809003807" Z. Marioli-Riga, Structural health monitoring of glass fiber reinforced composites using embedded carbon nanotube (CNT) fibers, Composites Science and Technology 70(2) (2010) 260–271.

[13] NASA, Multifunctional carbon nanotube yarn sensors, Advanced Sensing and Optical Measurement Branch. (Online) April 2008. (Cited: 2.1.2012.) http://asomb.larc.nasa.gov/research/nano_technology/yarn_sensors.htm.

[14] J.L. Abot, Z. Kier, V.N. Shanov, Y. Song, C. Jayasinghe, S. Sundaramurthy, M.J. Schulz, Self-sensing Composite Materials, UC 109–064 Provisional Patent (2009).

[15] H. Zhao, F. Yuan, Carbon nanotube yarn sensors for structural health monitoring of composites, SPIE, Nondestructive Characterization for Composite Materials, Aerospace Engineering, Civil Infrastructure, and Homeland Security, San Diego, CA, March 2011.

[16] X. Wang, D.D.L. Chung, Continuous carbon fibre epoxy-matrix composite as a sensor of its own strain, Smart Materials & Structures 5 (1996) 796–800.

[17] M.J. Schulz, A. Kelkar, M. Sundaresan, Nanoengineering of Structural, Functional, and Smart Materials, CRC Press, Boca Raton, 2006.

[18] Y. Song, Basics of carbon nanotube materials for structural applications, Nanotechnologies and smart materials for SHM, Ed. A. Catalano, G. Fabbrocino and C. Rainieri, ISBN 978-88-88102-47-4, Campobasso, Italy, 2012

[19] Y. Song, SHM applications of nanotechnologies for sensor development and communication, Nanotechnologies and smart materials for SHM, Ed. A. Catalano, G. Fabbrocino and C. Rainieri, ISBN 978-88-88102-47-4, Campobasso, Italy, 2012.

[20] C. Jayasinghe, W. Li, Y. Song, J.L. Abot, V.N. Shanov, S. Fialkova, S. Yarmolenko, S. Sundaramurthy, Y. Chen, W. Cho, S. Chakrabarti, G. Li, Y. Yun, M.J. Schulz, Nanotube responsive materials, MRS Bulletin 35 (9) (2010) 682–692.

[21] M.J. Schulz, G. Maheshwari, J. Abot, Y. Song, C. Jayasinghe, N. Mallik, V. Shanov, M. Dadhania, Y. Yun, S. Yarmolenko, J. Sankar, Responsive nanomaterials for engineering asset evaluation and condition monitoring, BNDT: Insight Journal (June 2008).

[22] Yi Song, Carbon Nanotube Materials for Smart Composites, 242nd ACS National Meeting, Denver, Colorado, August 28-September 1, 2011.

[23] D.B. Mast, C. Jayasinghe, S. Chakobarty, L. Li, Y. Chen, W. Cho, M.J. Schulz, V. Shanov, J. Abot, S. Pixley, Carbon Nanotube Threads, Yarns and Ribbons: Making the Transition from Materials to High Performance Devices for Defense Applications, Nano Technology for Defense Conference, Burlinghame, CA, April, 2009.

[24] N. Mallik, C. Jayasinghe, S. Chakraborty, P. Salunke, W. Li, W. Cho, L. Lee, E. Head, D. Hurd, J. Abot, Y. Song, V. Shanov, M.J. Schulz, Fabrication of threads from carbon nanotube arrays. New Delhi, India, Proceedings of Processing and Fabrication of Advanced Materials – XVII (December 2008).

[25] V.N. Shanov, G. Choi, G. Maheshwari, G. Seth, S. Chopra, G. Li, Y. Yun, J. Abot, M.J. Schulz, Structural Nanoskin Based on Carbon Nanosphere Chains, SPIE, Sensors and Smart Structures Technologies for Civil, Mechanical, and Aerospace Systems San Diego, CA, March 2007.

[26] N. Mallik, Carbon nanotube array based smart materials, in: M. Umerno, Prakash R. Somani (Eds.), Carbon Nanotubes: Synthesis, Properties and Applications, Applied Science Innovations Pvt. Ltd., India, 2009. (Chapter 16).

[27] Inpil Kang, Nanoengineering of sensory materials, in: Fu-Kuo Chang, Yozo Fujino, Christian Boller (Eds.), Encyclopedia of Structural Health Monitoring, Wiley, 2008.

[28] V. Shanov, J. Abot, Y. Song, M. Schulz, De-Icing of Solid Structures by Surface Heating Through CNT Thread and Ribbon, UC Invention disclosure 109–076 USA (9.4.2009).

[29] G. Maheshwari, J. Abot, A. Song, E. Head, V. Shanov, M. Schulz, C. Jayasinghe, P. Salunke, Y. Yun, Powering up nanoparticles: versatile carbon materials for use in engineering and medicine, SPIE Newsroom, http://dx.doi.org/10.1117/2.1200809.1305.

[30] J.L. Abot, Y. Song, M.J. Schulz, V.N. Shanov, Novel carbon nanotube array-reinforced laminated composite materials with higher interlaminar elastic properties, Composite Science and Technology 68 (13) (2008) 2755–2760.

[31] G. Maheshwari, J. Abot, A. Song, E. Head, V. Shanov, M. Schulz, C. Jayasinghe, P. Salunke, Y. Yun, Novel Carbon Nanotube Array-Reinforced Laminated Composite Material, SAMPE Conference, Cincinnati, OH, 2007.

[32] W. Li, J. Bulmer, B. Ruff, Y. Song, P. Salunke, V. Shanov, M.J. Schulz, Modeling the electrical impedance of carbon nanotube ribbon, Nano LIFE (May 2013).

[33] J.P.M. She, J.T.W. Yeow, Carbon nanotube-enhanced capillary condensation for a capacitive humidity sensor, Nanotechnology 17 (21) (2006).

[34] K. Chawla, Composite Materials, Second Ed., Springer, 1998.

[35] GamryInstruments. Application Note: Getting Started with Electrochemical corrosion measurement, http://www.gamry.com/assets/Application-Notes/Getting-Started-with-Electrochemical-Corrosion-Measurement.pdf.

[36] B. Suberu, Y. Song, V.N. Shanov, M.J. Schulz, High Volume Fraction Composite (HVFC), UC UC Invention Disclosure (28.4.2012) 112–088.

[37] J. Suhr, N. Koratkar, P. Keblinski, P. Ajayan, Viscoelasticity in carbon nanotube composites, Nature Materials 4 (2005) 134–137.

[38] X. Li, C. Levy, A. Agarwal, A. Datye, L. Elaadil, A.K. Keshri, M. Li, Multifunctional carbon nanotube film composite for structure health monitoring and damping, Open Construction and Building Technology Journal 3 (2009) 146–152.

[39] B.D. Agarwal, L.J. Broutman, K. Chandrashekhara, Analysis and Performance of Fiber Composites, Wiley, Hoboken NJ, 2006.

[40] R. Hollertz, S. Chatterjee, H. Gutmann, T. Geiger, F.A. Nüesch, B.T.T. Chu, Improvement of toughness and electrical properties of epoxy composites with carbon nanotubes prepared by industrially relevant processes, Nanotechnology 22 (12) (2011).
[41] R. Weisenberger, M.C. Andrews, Carbon nanotube polymer composites, Current Opinion in Solid State and Materials Science 8 (1) (2004) 31–37.
[42] S. Shaikh, K. Lafdi, A carbon nanotube-based composite for the thermal control of heat loads, Carbon 50 (2) (2012) 542–550.
[43] S.C. Jun, J.H. Choi, S.N. Cha, C.W. Baik, S. Lee, H.J. Kim, J. Hone, J.M. Kim, Radio-frequency transmission characteristics of a multi-walled carbon nanotube, Nanotechnology 18 (25) (2007).
[44] Y. Tzeng, T.S. Huang, Y.C. Chen, C. Y.K.
[45] R. Hu, B.A. Cola, N. Haram, J.N. Barisci, S. Lee, S. Stoughton, G. Wallace, C. Too, M. Thomas, A. Gestos, M.E.D. Cruz, J.P. Ferraris, A.A. Zakhidov, R.H. Baughman, Harvesting waste thermal energy using a carbon-nanotube-basedthermo-electrochemical cell, Nano Letters 10 (3) (2010) 838–846.
[46] Prashant V. Kamat, Harvesting photons with carbon nanotubes, Nano Today 1 (4) (2006) 20–27.
[47] NASA, DRAFT: Nanotechnology Road MapdTA10 (November 2010). http://www.nasa.gov/pdf/501325main_TA10-Nanotech-DRAFT-Nov2010-A.pdf.
[48] J.L. Abot, M.J. Schulz, Y. Song, S. Medikonda, N. Rooy, Novel distributed strain sensing in polymeric materials, Smart Materials & Structures 19 (8) (2010).
[49] J.L. Abot, Y. Song, M.S. Vatsavaya, S. Medikonda, Z. Kier, C. Jayasinghe, N. Rooy, V.N. Shanov, M.J. Schulz, Delamination detection with carbon nanotube thread in self-sensing composite materials, Composites Science and Technology 70 (7) (2010) 1113–1119.
[50] V. Shanov, C. Jayasinghe, J. Abot, Yi Song, M. Schulz, Remote, Non-Destructive Approach for Detecting Defects and Cracks in Solid Structures, UC Invention Disclosure (10.4.2009) 109–077.
[51] E.F. Northrup, Methods of Measuring Electrical Resistance, McGraw Hill, NY, 1912.
[52] W. Obitayo, T. Liu, A review: carbon nanotube-based piezoresistive strain sensors, Journal of Sensors (2012).
[53] M. Miao, J. McDonnell, L. Vuckovic, S.C. Hawkins, Poisson's ratio and porosity of carbon nanotube dry spun yarns, Carbon 48 (10) (2010) 2802–2811.
[54] J.J. Sullivan, A.J. Hehr, Effects of Thread Twist Angle on the Thread Properties: A Preliminary Study, Internal Report of Nanoworld Labs, University of Cincinnati, 2012.
[55] I.M. Daniel, O. Ishai, Engineering Mechanics of Composite Materials, NewYork, Oxford, 2006.
[56] Data Link. Wireless Multiplexer Product Info. (Online) (Cited: 16.11.2012) http://www.data-linc.com/dd1000.htm.
[57] F22 Specification Facts. (Online) (Cited: 6.10.2013) http://www.f22fighter.com/Specs.htm
[58] C.W.D. Silva, Damping. Vibration: Fundamentals and Practice, CRC Press, Boca Raton, 2000 Chapter 7.
[59] L.E. Nielsen, R.F. Landel, Mechanical Properties of Polymers and Composites, Marcel Dekker, Inc, NY, 1994.

Nanotube Superfiber Materials

Changing Engineering Design

Edited by

Mark J. Schulz

Vesselin N. Shanov

Zhangzhang Yin

ELSEVIER

AMSTERDAM • BOSTON • HEIDELBERG • LONDON
NEW YORK • OXFORD • PARIS • SAN DIEGO
SAN FRANCISCO • SINGAPORE • SYDNEY • TOKYO

William Andrew is an imprint of Elsevier

William Andrew is an imprint of Elsevier
The Boulevard, Langford Lane, Kidlington, Oxford OX5 1GB, UK
225 Wyman Street, Waltham, MA 02451, USA

First edition 2014

Notice
No responsibility is assumed by the publisher for any injury and/or damage to persons or property as a matter of products liability, negligence or otherwise, or from any use or operation of any methods, products, instructions or ideas contained in the material herein. Because of rapid advances in the medical sciences, in particular, independent verification of diagnoses and drug dosages should be made

British Library Cataloguing in Publication Data
A catalogue record for this book is available from the British Library

Library of Congress Cataloging-in-Publication Data
A catalog record for this book is availabe from the Library of Congress

ISBN–13: 978-1-4557-7863-8

Printed and bound in the US

13 14 15 16 17 10 9 8 7 6 5 4 3 2